

Temporal signatures of radiation belt electron precipitation induced by lightning-generated MR whistler waves: 1. Methodology

J. Bortnik,¹ U. S. Inan, and T. F. Bell

Space, Telecommunications, and Radioscience Laboratory, Department of Electrical Engineering, Stanford University, Palo Alto, California, USA

Received 11 April 2005; revised 16 November 2005; accepted 25 November 2005; published 21 February 2006.

[1] We present a novel technique designed to calculate the detailed differential number flux signature (as a function of energy and time) of precipitating radiation-belt electrons, driven by a magnetospherically reflecting (MR) whistler wave, initiated by a single cloud-to-ground lightning discharge. Our model consists of several stages. First, we calculate the MR whistler wave characteristics at 1° latitude intervals along a given field-line. This is accomplished using an extensive ray tracing and interpolation algorithm involving ~ 120 million rays, and accounting for the effects of Landau damping, spatial, and temporal dispersion. We then use these wave characteristics to compute the pitch angle changes of resonant electrons by assuming that the interactions are linear, and independent between adjacent latitude and wave frequency bins. The pitch angle changes are transformed to precipitating flux using a novel convolution method and displayed as a function of particle energy and time at the feet of a given field line. We have calculated and compared the differential number flux signatures at the northern and southern feet of the $L = 2.3$ and $L = 3$ field lines, and found that precipitation onset and duration times increase with latitude (consistent with previous work). The precipitation consists of suprathermal Landau resonance electrons ($E \lesssim 10$ keV) which are intense but contribute little to the total energy flux, a flux gap ($10 \text{ keV} \lesssim E \lesssim 80 \text{ keV}$) corresponding to a change in coupling mechanism from Landau resonance to gyroresonance, and a series of precipitation swaths ($E \gtrsim 80 \text{ keV}$) corresponding to gyroresonance interactions. The swaths result in periodic maxima in the precipitated energy flux, which correspond to the equatorial traversals of the underlying MR whistler wave energy. Global precipitation signatures were computed for a number of lightning discharge latitudes and are presented in a companion paper (Bortnik et al., 2006).

Citation: Bortnik, J., U. S. Inan, and T. F. Bell (2006), Temporal signatures of radiation belt electron precipitation induced by lightning-generated MR whistler waves: 1. Methodology, *J. Geophys. Res.*, *111*, A02204, doi:10.1029/2005JA011182.

1. Introduction

[2] Recent observations made in space aboard the SAMPEX (Solar, Anomalous, and Magnetospheric Particle EXplorer) satellite [Blake et al., 2001] and on the ground with the HAIL (Holographic Array for Ionospheric Lightning) network [Johnson et al., 1999; Peter and Inan, 2004] suggest that pitch-angle scattering by nonducted whistlers can be an important loss mechanism for energetic radiation belt electrons.

[3] Electron precipitation driven by lightning-generated obliquely propagating whistler waves has been studied by numerous workers [Bell, 1984; Jasna et al., 1992; Abel and

Thorne, 1998a, 1998b; Johnson et al., 1999; Lauben, 1999; Lauben et al., 2001; Blake et al., 2001; Bortnik et al., 2002a, 2002b; Clilverd et al., 2002] who considered either the first hop of the whistler, only the Magnetospherically Reflecting (MR) portion of the wave, or the equilibrium flux of energetic particles. In this work we calculate the detailed temporal behavior of the differential flux of precipitating radiation belt electrons driven by an MR whistler produced by a single cloud to ground lightning discharge, accounting for the complete temporal development of the precipitation from the point of injection of the wave to the point at which the wave energy is damped to negligible levels.

[4] The MR whistler driven scattering process proceeds as follows: first, a lightning discharge radiates ELF and VLF electromagnetic waves into the Earth-ionosphere waveguide which propagate away from the source, illuminating a large region of the bottomside ionosphere [Crory, 1961]. A portion of the radiation incident on the bottomside

¹Now at Department of Atmospheric and Oceanic Sciences, University of California, Los Angeles, California, USA.

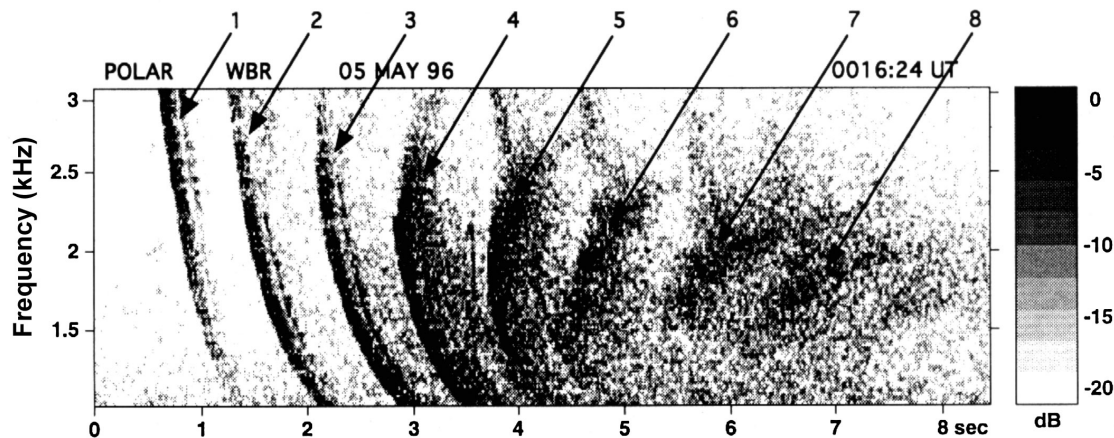


Figure 1. MR whistler observed aboard the POLAR satellite in the 8 sec interval starting at 0016:24 UT on May 5, 1996, showing 8 distinct components.

ionosphere leaks through to the topside ionosphere, experiencing collisional losses along the way, and coupling into the whistler mode of propagation [Helliwell, 1965, p. 71]. The whistler wave then propagates away from the Earth in the nonducted mode, being refracted by the gradients in the magnetic field \mathbf{B}_0 and electron number density n_0 [Edgar, 1972]. Near the point at which the wave frequency is equal to the local lower hybrid frequency, these gradients can lead to the rotation of the wave vector beyond 90° with respect to \mathbf{B}_0 [Kimura, 1966], causing the whistler to reverse its direction of propagation (commonly referred to as a magnetospheric reflection). The process of propagation and reflection can occur several times before the MR whistler is absorbed by suprathermal (~ 100 eV–1 keV) electrons through Landau damping. An example of an MR whistler observed aboard the POLAR satellite is given in Figure 1 showing multiple reflections of the wave packet, and the ray path of a 3 kHz ray together with the path integrated Landau damping is illustrated in Figure 2.

[5] As the MR whistler propagates it alters the pitch-angles of energetic electrons through both gyroresonance and Landau resonance interactions. These interactions are strongest near the magnetic equatorial plane, and slightly modify the pitch-angle of the resonant electrons, causing some electrons with pitch-angles on the edge of the loss-cone to have their pitch angle lowered and precipitate into the dense upper atmosphere within one bounce period [Inan *et al.*, 1978]. Since the primary geomagnetic dipole field is slightly eccentric [Bartels, 1936], resonant electrons whose pitch-angles are not lowered into the bounce loss-cone may nevertheless be lost from the radiation-belts within one drift period around the Earth (i.e., whose pitch-angles enter the drift-loss-cone), as discussed by Blake *et al.* [2001]; however, in this paper we focus entirely on the former case dealing with precipitation in the bounce-loss-cone.

[6] The remainder of this paper is divided into three sections, presenting our method (section 2), results (section 3), and conclusions (section 4). In section 2.1 we briefly review the methodology used to simulate the MR whistler wave presented by Bortnik *et al.* [2003b]; we then discuss our new technique used in calculating the pitch-angle changes of resonant energetic electrons (section 2.2), and a novel method to calculate the resulting precipitated

flux of electrons due to the MR whistler wave (section 2.3) which uses a convolution approach. In section 2.4, we present the model we used to simulate the trapped particle flux, which is based on the AE8 MAX model, and includes a realistic pitch-angle distribution.

[7] In section 3 we show the results of our simulation, including the precipitated differential number flux of electrons at the northern and southern feet of the $L = 2.3$ and $L = 3$ field lines, as well as the energy flux. We highlight the important features of these results and discuss the driving physical mechanisms responsible for their formation. We conclude the paper in section 4 giving a summary of our work and major findings.

2. Wave-Particle Interaction Model

[8] The wave-particle interaction model entails (1) the specification of the whistler wave characteristics along a particular field-line (section 2.1), and (2) the calculation of the precipitated flux driven by the wave (sections 2.2 and 2.3) along that field line. In calculating the pitch-angle scattering of resonant particles, we neglect the feedback of the particles on the wave (i.e., the re-radiated fields). This assumption is consistent with past work [Inan *et al.*, 1978, 1982; Chang and Inan, 1983a, 1983b; Chang *et al.*, 1983; Chang and Inan, 1985a, 1985b; Inan *et al.*, 1985; Neubert *et al.*, 1987; Jasna, 1993; Lauben, 1999; Lauben *et al.*,

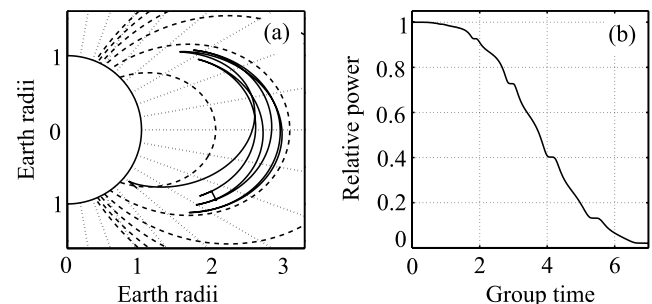


Figure 2. (a) The ray path of a 3 kHz whistler-mode ray injected at -40° latitude, showing multiple magnetospheric reflections, and (b) the relative power of the ray as a function of time.

Table 1. Summary of Key Wave Characteristics Used in the MR Whistler Wave Simulation

Parameter	Value
Frequency range	200 Hz–60 kHz
Source latitude, λ_s	35°
Latitudinal range	$\pm 10^\circ$ about λ_s
Ray paths	41 rays per frequency component, 130 frequency components (5330 total ray paths)
Interpolation	0.01° in injection latitude every 1 Hz in frequency (~120 million interpolated rays paths)
Pulse length	20 μ s rise time to peak; 180 μ s fall time to 50% of peak
Peak amplitude	8.5 kA maximum
Plasmasphere	<i>Carpenter and Anderson</i> [1992] model with $K_{p,max} = 0$ corresponding to $L_{pp} \sim 5.5$

2001] and is considered valid when relatively weak waves are involved (wave magnetic-field component $B^w \lesssim 1$ pT) as in the present case, so that no phase trapping occurs [Bell, 1986]. For example, *Inan et al.* [1978] estimated that under the ‘smoothest’ conditions (i.e., monochromatic, parallel propagating whistlers) phase trapping would begin at ~ 50 pT and nonlinear effects would become more prevalent for $B^w \gtrsim 7$ pT, although the nonlinear RMS pitch-angle scattering does not begin to significantly deviate from the linear case until $B^w \gtrsim 20$ pT [Inan et al., 1978]. In our case, due to additional spatiotemporal gradients in wave number \mathbf{k} and wave frequency f , the interaction lengths become even shorter allowing less opportunity for non-linear effects.

[9] In effect, even if some amplification of the wave is present, as argued by *Inan et al.* [1978] there is no need to perform a self-consistent simulation since we are only concerned with particles near the edge of the loss-cone in this work (within $\sim 1^\circ$), and the particle population responsible for wave-growth consists of particles with higher pitch-angles. In the case of MR whistlers which are confined to the plasmasphere, and the ratio of plasma frequency to gyrofrequency is always greater than 10, it can be shown [Glauert and Horne, 2005] that the energy diffusion coefficient peaks at $\alpha = 60^\circ - 90^\circ$, i.e., well away from the loss-cone. Since satellite observations of MR whistlers show that these waves typically do not exhibit evidence of wave growth and triggering of VLF emissions [Edgar, 1972], our test-particle approach seems reasonable.

2.1. Wave Characteristics Along a Single Field Line

[10] We use the methodology and parameter values described by *Bortnik et al.* [2003b] and briefly repeated below, to calculate the detailed frequency-time ($f - t$) spectra of each MR whistler as observed at 1° latitude intervals along the field-lines of interest.

[11] The lightning discharge is modeled as a short, vertical current above the ground [Lauben et al., 2001; Bortnik et al., 2003a, 2003b] which allows us to analytically specify the upgoing VLF wave power at the bottomside ionosphere (100 km) as a function of radial distance from the source. The wave power at the bottomside ionosphere is then translated to the topside ionosphere (1000 km) by multiplying it with a transionospheric propagation damping constant [Helliwell, 1965, Figures 3–35], which is depen-

dent on wave frequency and geographic latitude. The above procedure gives a complete specification of the wave power at the topside ionosphere, which we use to ‘weight’ each ray in our raytracing, before its ray path and Landau damping is calculated.

[12] To obtain observations of our simulated MR whistler wave packet, we define an effective area perpendicular to the field line at each observation point, and use ray tracing and interpolation to determine the ray paths of ~ 120 million ray paths. We then simply record the characteristics of waves that cross our defined effective area and bin these characteristics according to their frequency and time (bin widths are $\Delta f = 10$ Hz, $\Delta t = 10$ ms). A number of key parameters describing our wave simulation are given in Table 1, and a detailed description together with example spectrograms and typical wave power is given in *Bortnik et al.* [2003b].

[13] The level of latitude discretization (i.e., the spectrograms recorded at 1° intervals) is chosen to give the highest sampling rate of the field line possible, given our available computational resources, and ensuring a smooth progression of the recorded wave characteristics with latitude and time. To ensure ‘smoothness’ we require that the whistler wave packet should propagate between adjacent latitude bins (i.e., from $\lambda_{i\pm 1}$ to λ_i) in approximately one time bin, Δt , of the $f - t$ spectra we construct. Since we consider a large distribution of wave frequencies (ω), wave normal angles (θ), plasma (ω_p) and gyro-frequencies (ω_H), each combination of (ω , θ , ω_p , ω_H) results in a different value of the refractive index and hence different phase and group velocities of the wave. However, for typical parameters used in our simulation, refractive index values of $\mu = 10 - 100$ satisfy our smoothness criterion over the L -shells of interest ($L \lesssim 6$).

[14] Although typical coherent interaction lengths span a few degrees in latitude for monochromatic parallel propagating whistler waves [Helliwell, 1967; Inan et al., 1983], the interaction lengths for most of the particles are generally less for obliquely propagating, variable frequency waves due to the additional gradients in \mathbf{k} -vector and frequency. Our choice of 1° latitude bins represents a realistic interaction length, which is extended by a factor of 2 (effectively a 2° interaction length) in a ‘windowing’ operation (section 2.2). This choice allows for effective sampling of the wave characteristics along the field line and results in reasonable computation times.

[15] At every $f - t$ bin of the simulated spectrogram we record the parameters necessary for the calculation of wave-induced pitch angle change as a function of time (e.g., wave frequency, wave power density, wave normal angle, group time, etc.). The resulting set of calculated $f - t$ spectra effectively provide an approximation of the wave structure experienced by trapped electrons moving between mirror points in the northern and southern hemisphere. In each latitude bin the MR whistler frequency spectrum is quantized into a series of frequencies separated by $\Delta f = 10$ Hz.

2.2. Calculation of the Change in Pitch-Angle

[16] We now use the wave characteristics computed as described above to calculate the differential number flux of electrons precipitating into the upper ionosphere. To do this we assume that the pitch-angle changes of energetic elec-

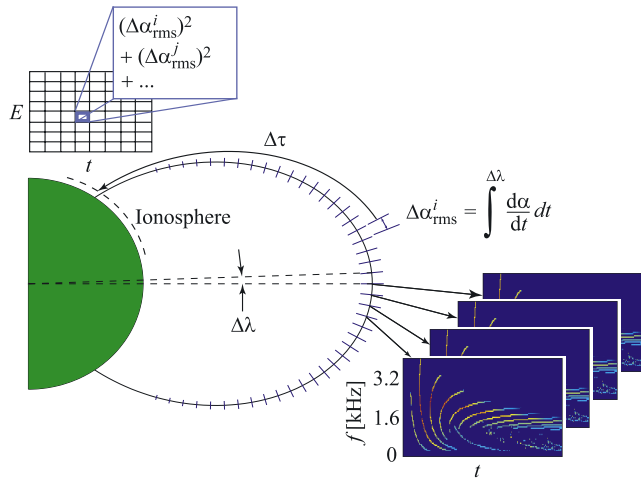


Figure 3. Illustration of flux calculation technique: calculate a pitch-angle change $\Delta\alpha_i$, and flight time to ionosphere $\Delta\tau$, for each $f - t$ cell in the spectrogram for each resonance mode, over all latitudes; add $(\Delta\alpha_{rms}^i)^2$ into the appropriate energy-arrival time bin at the ionosphere.

trons due to the different frequency components that constitute the wave packet (i.e., the $f - t$ spectra, divided into $\Delta f = 10$ Hz bins) in each 1° latitude bin are not correlated. Clearly, this assumption is not strictly true; however, we show below that the impact of any correlation upon the measurable precipitated flux signatures is minimal. As discussed by *Lauben et al.* [2001], when interacting with a nonducted whistler wave packet at least some portion of the particle population may enter the wave packet in a specific location and with such a velocity and pitch-angle that the interactions with the different frequency components are phase coherent and thus cumulative (i.e., the variations in the medium parameters such as ω_H , ω_p are just compensated by the variations in the wave frequency and \mathbf{k} -vector), resulting in an unusually high pitch-angle perturbation, much higher than can be accounted for on the basis of linear theory alone. Fortunately, as shown in *Lauben* [1999] and as discussed below, the number of particles that can coherently resonate with the variable frequency wave is quite small. As a result, the precipitation flux associated with this portion of the particle population is negligible compared with that constituted by the remainder

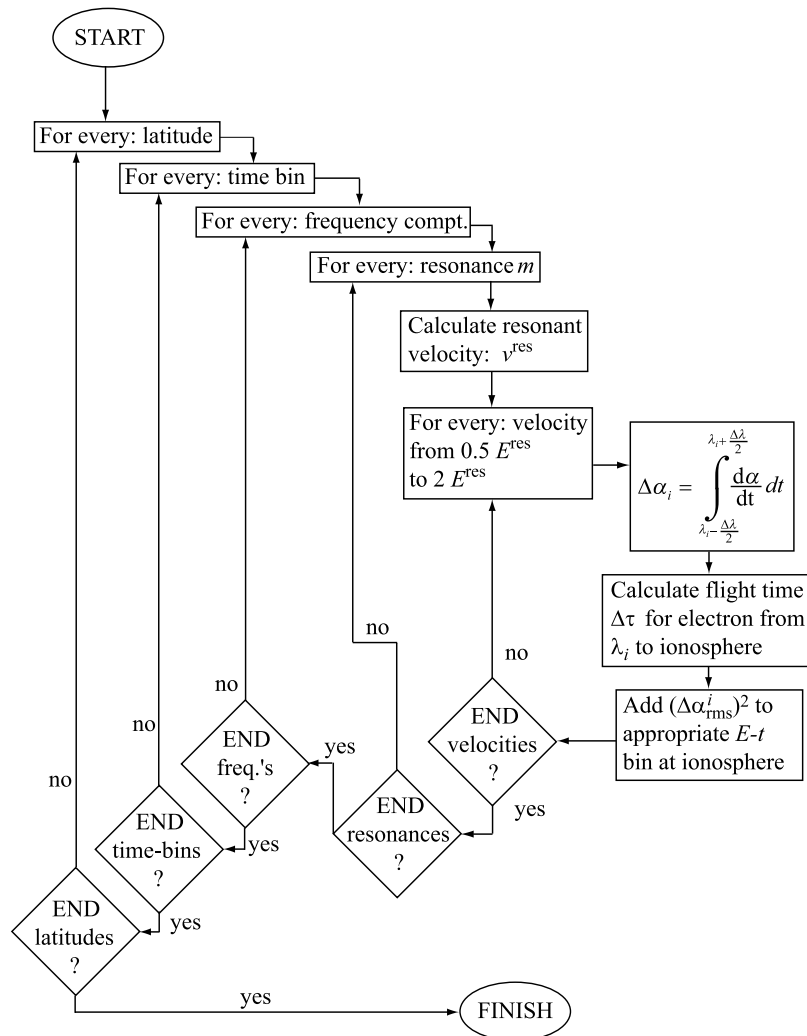


Figure 4. Flowchart illustrating the procedure of calculating the pitch angle changes at the ionosphere of resonant particles, as a function of energy and time of arrival.

of the particles which essentially undergo a random walk in pitch angle in the wave packet, and the interactions of which can be handled using a linear diffusion analysis. The assumption of uncorrelated pitch-angle changes due to different wave frequency components at a given point and between interactions which occur at different latitude bins is important in our work, because it allows extensive parallelization of the problem, essentially making it solvable within present computational resources.

[17] Figures 3 and 4 illustrate in graphical and flowchart form the procedure used in calculating the pitch-angle changes of resonant particles as described below. We build a table of pitch-angle changes (referred to the magnetic equator) acquired by resonantly interacting electrons, displayed as a function of particle energy and time-of-arrival at the ionosphere. Thus, we separately treat the scattering produced by wave energy represented by every $f - t$ cell in each spectrogram at each latitude bin, and evaluate the resonant velocity for a particular harmonic resonance mode. This procedure is repeated for each harmonic resonance mode ranging from -5 to 5 , for time bins ranging from 0 to 20 sec (where the source lightning discharge occurs at $t = 0$), for frequency bins ranging from 200 Hz to 60 kHz, and for geomagnetic latitude bins ranging from -40° to 40° along the field line.

[18] The resonant electron velocity is calculated from the well-known relativistic gyro-resonance condition [Chang and Inan, 1983a], by setting $d\eta/dt \approx 0$ where:

$$\frac{d\eta}{dt} = \omega + v_z^{\text{res}} k_z - m\omega_H/\gamma \quad (1)$$

and η is the angle between the wave magnetic field vector and the particle velocity perpendicular to \mathbf{B}_0 , ω and ω_H are the wave and gyrofrequencies, respectively, v_z^{res} and k_z are the resonant velocity and wave number components, respectively, that are parallel to \mathbf{B}_0 , m is the gyro-harmonic order, and $\gamma = (1 - (v^{\text{res}}/c)^2)^{-1/2}$ is the relativistic Lorentz factor. Furthermore, for the present paper we consider only particles at the edge of the loss-cone [i.e., $v_z^{\text{res}} = v_z^{\text{res}}/\cos(\alpha_{1c})$]. The explicit expression for parallel resonant velocity is then given by:

$$v_z^{\text{res}} = \frac{\pm \sqrt{\omega^2 k_z^2 + [(m\omega_H)^2 - \omega^2] \left[k_z^2 + \left(\frac{m\omega_H}{c \cos \alpha_{1c}} \right)^2 \right]} - \omega k_z}{k_z^2 + \left(\frac{m\omega_H}{c \cos \alpha_{1c}} \right)^2} \quad (2)$$

where the \pm sign on the radical indicates the direction of travel of the particle, the $+(-)$ indicating counter-streaming (co-streaming) particles and must be used with positive (negative) m . We define a band of velocities corresponding to a range of energies a factor of two about the resonant energy, calculated using (2), discretize the band and evaluate the pitch angle change for each velocity as described below. For reference, a factor of two in energy at 300 keV (i.e., 150 keV to 600 keV) corresponds to velocity bounds of -29.5% to $+41.4\%$ of v^{res} . We choose to work with energy bounds instead of velocity bounds

because the velocity bounds becomes less accurate as particle resonant energies become more relativistic ($v^{\text{res}} \rightarrow c$), with very small changes in velocity translating to large changes in energy.

[19] The rate of pitch-angle (α) change as a function of time (t) of a particle moving through an oblique whistler wave-field was described by Bell [1984, equation (47)] and is rewritten below for the relativistic case as:

$$\frac{d\alpha}{dt} = \underbrace{-\frac{m_e \omega_{\tau m}^2}{k_z p_\perp} \left(1 + \frac{\cos^2 \alpha}{mY - 1} \right)}_{T_1} \underbrace{\sin \eta}_{T_2} + \underbrace{\frac{1}{m_e \gamma} \frac{p_\perp}{2\omega_H} \frac{\partial \omega_H}{\partial z}}_{T_3} \quad (3)$$

where $Y = \omega_H/\omega$, p_\perp and m_e are the electron's momentum perpendicular to the ambient magnetic field and rest mass, respectively, and:

$$\beta = \frac{k_x p_\perp}{m_e \gamma \omega_H} \quad (4)$$

$$k_z = k \cos \theta = (\omega \mu / c) \cos \theta; \quad k_x = k \sin \theta \quad (5)$$

$$\omega_{\tau m}^2 = (-1)^{m-1} \omega_{\tau 0}^2 [J_{m-1}(\beta) - \alpha_1 J_{m+1}(\beta) + \gamma \alpha_2 J_m(\beta)] \quad (6)$$

$$\omega_{\tau 0}^2 = \frac{\omega_1 k_z p_\perp}{\gamma m_e} \quad (7)$$

$$\omega_1 = \frac{e}{2m_e} (B_x^w + B_y^w); \quad \omega_2 = \frac{e}{2m_e} (B_x^w - B_y^w) \quad (8)$$

$$\alpha_1 = \frac{\omega_2}{\omega_1}; \quad \alpha_2 = \frac{e E_z^w}{\omega_1 p_\perp} \quad (9)$$

$$R_1 = \frac{E_x^w + E_y^w}{B_x^w + B_y^w}; \quad R_2 = \frac{E_x^w - E_y^w}{B_x^w - B_y^w} \quad (10)$$

where $E_{x,y,z}^w$ and $B_{x,y,z}^w$ are the real values of the wave electric and magnetic fields in the x , y , and z directions, respectively, e is the electron charge, i.e., $e = |q| = 1.6 \times 10^{-19}$ C, and J_i are Bessel functions of the first kind, order i . We note that the direction vectors x , y , and z , refer respectively to the direction of the static magnetic field, direction of increasing L -shell, and y completes the right-handed set.

[20] To close our set of equations, we note that the wave electric and magnetic field components in (10) are not independent, but are instead related through the physics of the propagation mode. Following previous work [Bell, 1984; Jasna, 1993; Lauben et al., 2001; Bortnik, 2004], we relate the Poynting flux of the wave $\mathbf{S}^w = (1/2) \Re \mathbf{E}^w \times \mathbf{H}^w$, as well as all other wave components to the single reference component B_y^w as:

$$|B_y^w|^2 = \frac{2\mu_0 \rho_2^2 X^2 \mu \cos \theta |\mathbf{S}^w|}{c \sqrt{(\tan \theta - \rho_1 \rho_2 X)^2 + (1 + \rho_2^2 X)^2}} \quad (11)$$

$$X = \frac{P}{P - \mu^2 \sin^2 \theta} \quad (12a)$$

$$\rho_1 = \frac{E_z^w}{E_y^w} = \frac{(\mu^2 - S)\mu^2 \sin \theta \cos \theta}{D(\mu^2 \sin^2 \theta - P)} \quad (12b)$$

$$\rho_2 = \frac{E_x^w}{E_y^w} = \frac{\mu^2 - S}{D} \quad (12c)$$

and

$$\begin{aligned} \frac{E_x^w}{B_y^w} &= \frac{c(P - \mu^2 \sin^2 \theta)}{P\mu \cos \theta}, \\ \frac{E_y^w}{B_y^w} &= \frac{Dc(P - \mu^2 \sin^2 \theta)}{P\mu \cos \theta(S - \mu^2)}, \\ \frac{E_z^w}{B_y^w} &= \frac{-c\mu \sin \theta}{P}, \\ \frac{B_x^w}{B_y^w} &= \frac{-D(P - \mu^2 \sin^2 \theta)}{P(S - \mu^2)}, \\ \frac{B_z^w}{B_y^w} &= \frac{D \sin \theta (P - \mu^2 \sin^2 \theta)}{P \cos \theta (S - \mu^2)} \end{aligned} \quad (13)$$

where c is the speed of light, $\mu_0 = 4 \pi \times 10^{-7}$ H/m is the permeability of free space, and all other symbols have been previously defined.

[21] Equation (3) is integrated about the latitude of interest λ_i , from $\lambda_i - \Delta\lambda/2$ to $\lambda_i + \Delta\lambda/2$ where $\Delta\lambda$ in our case is taken to be 1° . Specifically, to perform the integration we divide (3) into three parts labeled T_1 , T_2 , and T_3 . The term T_3 describes adiabatic motion and is implicitly incorporated when we refer the change in pitch angle to its geomagnetic equatorial value.

[22] The factor T_1 generally varies slowly in the interval of interest, so we treat it as a constant evaluated at λ_i . The factor T_2 is the fastest varying of the factors in Equation (3), and typically undergoes many cycles in an integration interval unless the resonance condition (2) is approximately satisfied, in which case η remains approximately constant.

[23] For simplicity, we approximate the gyrofrequency as a linear function in z (distance along the field line) at the center of each latitude bin λ_i , i.e., $\omega_H \simeq \omega_H(\lambda_i) + (\partial\omega_H/\partial z)|_{\lambda=\lambda_i}(z - z_0)$ so that η becomes quadratic in z , and the integral of T_2 can generally be evaluated in the form of Fresnel integrals which are readily solved using a fast numerical technique [Mielenz, 2000]. In the integration of (3) p_\perp is also approximated to first order to be the adiabatically varying unperturbed momentum, so that nonlinearities due to the wave forces are not included and the equation is integrable in terms of known functions (see similar past work such as Das [1971] and Ashour-Abdalla [1972]).

[24] Figure 5 shows the equatorial root-mean-square (rms) pitch-angle change of a group of monoenergetic electrons having the same pitch-angle, but being uniformly distributed in Larmor phase about B_0 (gyrotropic). These

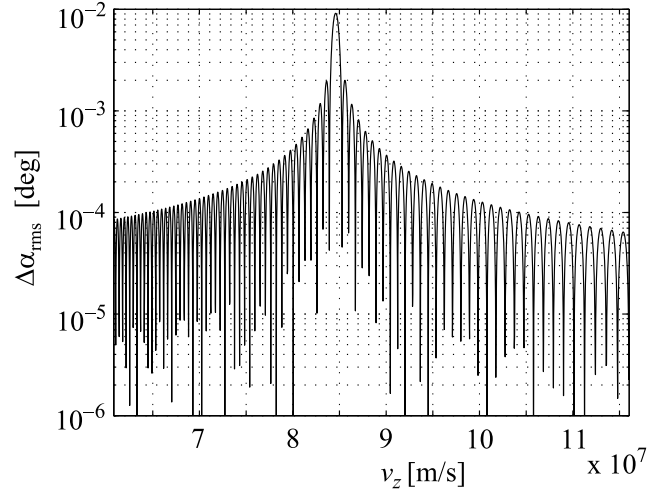


Figure 5. Equatorial rms pitch-angle change ($\Delta\alpha_{\text{rms}}$) as a function of electron parallel velocity v_z for a single $f - t$ cell at $\lambda_i = 0^\circ$.

particles move through a wave described by a single $f - t$ cell, at the magnetic equator ($\lambda_i = 0^\circ$), with $f = 3.055$ kHz, and $t = 0.935$ sec. In this figure, the resonant energy $E^{\text{res}} = 21.6$ keV ($v^{\text{res}} = 8.46 \times 10^7$ m/s) and the band of velocities considered corresponds to the energy range 10.8 keV to 43.2 keV, a wave normal angle $\theta = 58.32^\circ$, a refractive index $\mu = 63$, $B_y^w = 0.37$ pT, and $L = 3$. The figure indicates that the change in pitch-angle drops off rapidly as the velocity of the interacting electron deviates away from the resonance velocity. Due to this fast dropoff, in past work dealing with coherent wave-particle interactions the pitch-angle change was calculated for only a small band of electron velocities, typically 1%–3% [Inan et al., 1978; Chang and Inan, 1983a, 1983b, 1985a, 1985b; Jasna, 1993; Lauben et al., 2001] around the resonant velocity. Nevertheless, in this work we choose a broader band of velocities to ensure that “off-resonant pitch-angle changes are accounted for, since these can lead to increased precipitation fluxes [Wykes et al., 2001a, 2001b]. Our choice of the broad bounds for the energy range was made because at those bounds the pitch-angle deflection is ~ 100 times smaller than at the resonant velocity and hence can be considered negligible. In actual fact, the most significant contribution to precipitated flux comes from those electrons within a few percent of the resonant velocity, so our choice of a factor of two (in energy) is quite sufficient.

[25] The quasi-periodic nulls in pitch-angle deflection shown in Figure 5 are caused by the artificially imposed sharp limit on the wave-particle interaction length, due to our latitude “binning”. While it is more accurate to consider the envelope of pitch-angle deflections (thus avoiding the nulls), a preliminary analysis shows that after adding the pitch angle contributions from all $f - t$ bins at all latitudes, the effect of this artificiality is rendered insignificant so the enveloping operation can be omitted for computational simplicity.

[26] Figure 6 shows an example of a comparison of our analytical solution (blue curve) to the full solution (red curve) of (3) over two different 1° latitude bins, at $\lambda_i = 0^\circ$

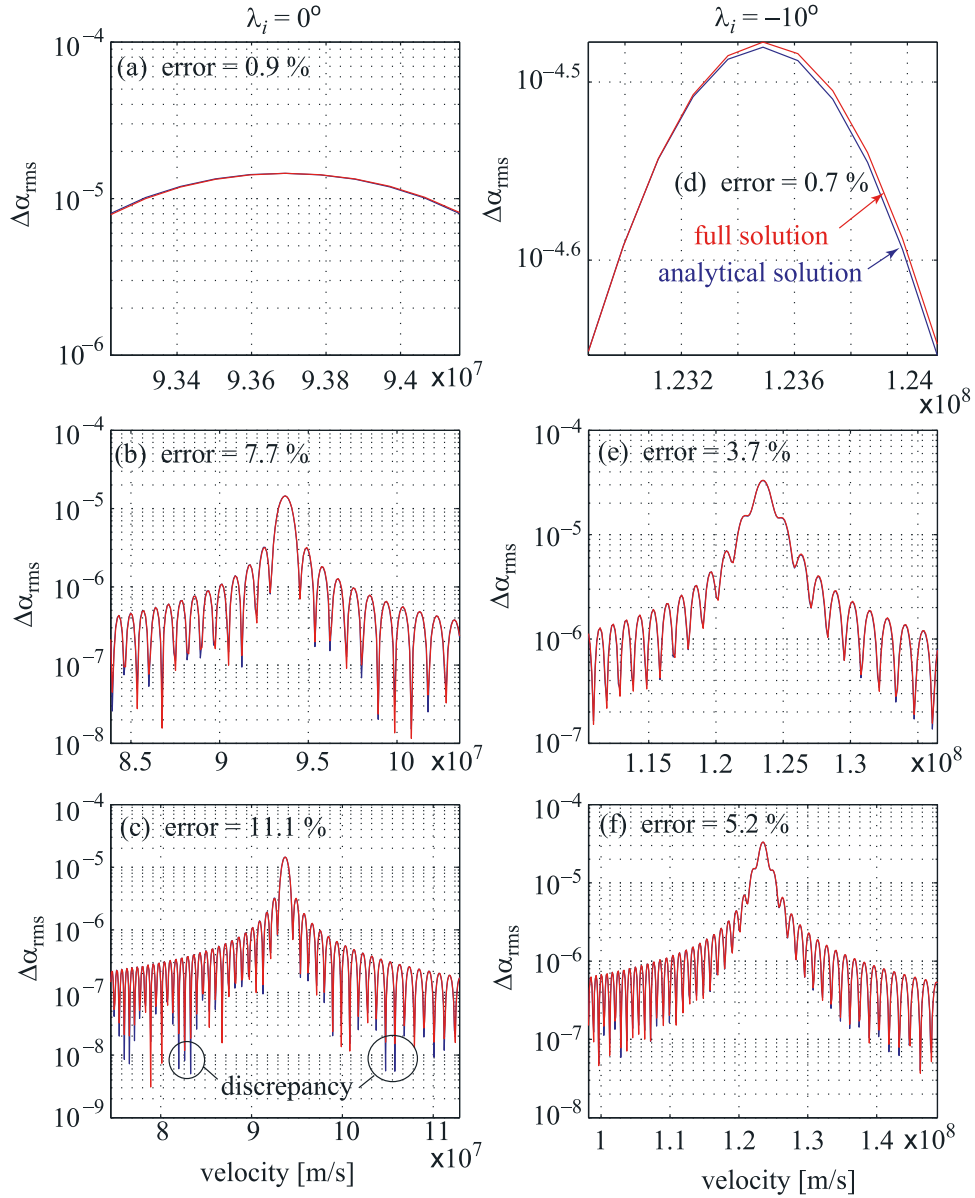


Figure 6. Comparison of $\Delta\alpha_{\text{rms}}$ using analytical (blue) versus full non-linear solution (red) methods, at two different latitude bins $\lambda_i = 0^\circ$ (left column) and $\lambda_i = -10^\circ$ (right column), using three different velocity bands about the resonant velocity, $\pm 0.5\%$, $\pm 10\%$, and $\pm 20\%$ in rows 1, 2, and 3, respectively.

(left column), and $\lambda_i = -10^\circ$ (right column). The full solution is obtained by integrating (3) with (1) and (10) numerically over the entire 1° latitude bin, explicitly calculating the values of all the terms in the integration without resorting to the analytical simplifications described above in connection with the analytical solution. We consider three velocity ranges around the resonant velocity, $\pm 0.5\%$, $\pm 10\%$, and $\pm 20\%$ in rows 1, 2, and 3, respectively, and compute the average error in each band as:

$$\text{Error} = \frac{1}{v_2 - v_1} \sum_{v_1}^{v_2} \frac{|\Delta\alpha_{\text{rms}}^{\text{analyt}} - \Delta\alpha_{\text{rms}}^{\text{full}}|}{\Delta\alpha_{\text{rms}}^{\text{full}}} \quad (14)$$

where v_1 and v_2 are the lower and upper velocity bounds, respectively, around the resonant velocity.

[27] The figure shows that typical errors between our analytical solution and the full solution are $< 1\%$ for velocities near the resonant velocity (Figures 6a and 6d), and increase as the range of velocities around the resonant velocity is increased, as in Figures 6b and 6c and Figures 6e and 6f. This decrease in accuracy occurs primarily due to the formation of nulls as discussed in connection with Figure 5, where the deflection in pitch-angle is very sensitive to minor changes in the initial values (labeled as ‘discrepancy’ in our figure). The errors associated with points close to the nulls can be as large as 50%, but this does not impact our calculation since the absolute values of $\Delta\alpha_{\text{rms}}$ are extremely low compared to the peak, regardless of the method used in calculating them.

[28] As λ_i increases, the agreement between the two methods improves, and the error decreases regardless of

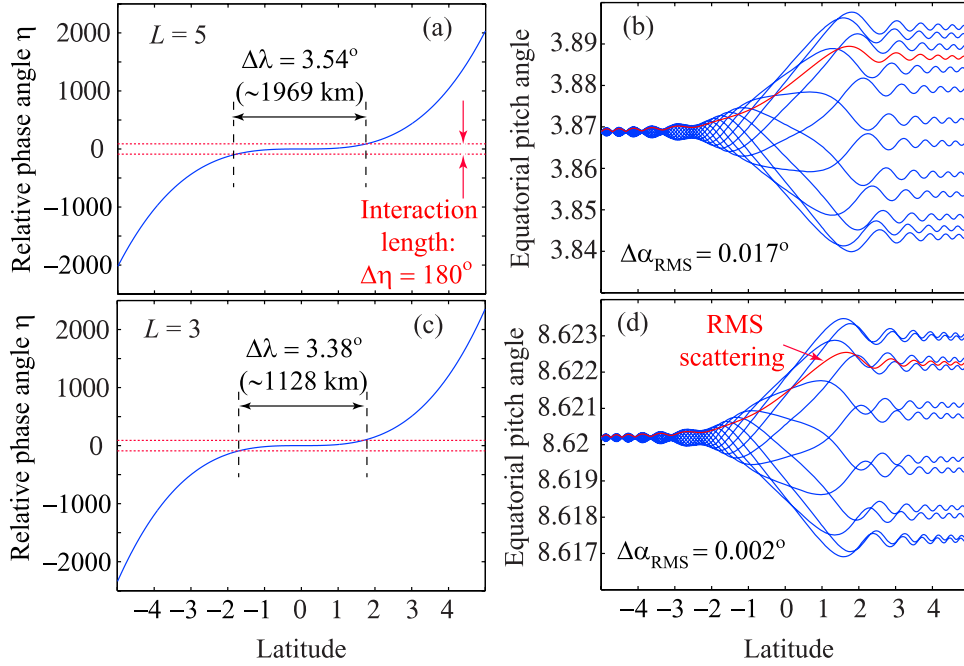


Figure 7. The resonant interaction of an energetic particle with an oblique whistler showing the relative phase angle η and equatorial pitch angle change at (a), (b) $L = 5$ and (c), (d) $L = 3$.

the velocity band used. This result comes about because the rate of change of \mathbf{B}_0 , v_z , and v_\perp with latitude is dominated by the first derivative which we account for in our analytical solution, compared with the second derivative which we neglect, and which is most important at the geomagnetic equator where the first derivative of the above quantities is zero (with respect to latitude).

[29] In integrating (1) to obtain η which is used subsequently in (3), we are left with the integration constant η_0 , which is the initial electron Larmor phase angle relative to the wave magnetic field. In past work [Inan *et al.*, 1978; Chang and Inan, 1985b; Inan *et al.*, 1985; Jasna, 1993; Lauben *et al.*, 2001], dependence of scattering on η_0 was accounted for explicitly by evaluating the equations of motion for 12 or more particles distributed uniformly in Larmor phase, since non-linear effects depend strongly on the relative phase between the particle and the wave. In our case, the interaction is assumed to be linear, in which case the scattering in pitch angle is proportional to $\sin\eta_0$ [Inan *et al.*, 1978] (with derivation in Appendix A of Inan [1977]). This sinusoidal dependence on η_0 provides for a number of analytical conveniences. Firstly, we need only solve (3) once (after averaging over initial Larmor phase) which directly gives the root-mean-square (rms) pitch-angle scattering $\Delta\alpha_{\text{rms}}$. Using $\Delta\alpha_{\text{rms}}$ we are able to characterize the entire interaction in Larmor phase (for example $\Delta\alpha_{\text{max}} = \sqrt{2}\Delta\alpha_{\text{rms}}$). Secondly, the uniform pitch-angle distribution of the particles in Larmor phase can be thought of as a random variable, which (when scattered by the wave) goes through a particular function (or filter) and attains a new distribution in pitch-angle. The probability density function (PDF) of this new distribution is discussed in section 2.3.

[30] After calculating the rms pitch angle change of a group of particles of a certain velocity at some given latitude λ_i , the flight time to the ionosphere $\Delta\tau$ is calculated

and the quantity $\Delta\alpha_{\text{rms}}^i = \sqrt{\langle(\Delta\alpha_i)^2\rangle}$ is referred to the equator (described below) and added into the appropriate energy-time ($E - t$) bin, where E is the particular energy of the group of particles under consideration, and t is the total time taken for the particle to reach the ionosphere from the time of origin of the source lightning discharge (i.e., the time for the whistler wave to propagate from the source to the given L -shell and latitude λ_i , plus the time taken for the electron to reach the topside ionosphere from this interaction latitude on that L -shell). The quantity $\Delta\alpha_{\text{rms}}^i$ is referred to the equator by adding it to the loss cone pitch-angle at λ_i , i.e., $\alpha_1 = \alpha_{\text{lc}}^i + \Delta\alpha_{\text{rms}}$, adiabatically mapping the sum to the equator using $\sin(\alpha_2)^2/B_{\text{eq}} = \sin(\alpha_1)^2/B_i$, and subtracting the equatorial loss-cone pitch angle $\Delta\alpha_{\text{rms}}^{\text{eq}} = \alpha_2 - \alpha_{\text{eq}}$. The behavior of a resonant particle near the equator is discussed below in connection with Figure 7.

[31] There are a number of important elements which underlie the methodology outlined above. Firstly, the pitch angle deflections $\Delta\alpha_{\text{rms}}^i$ that occur at different latitudes along the field-line, at different times, due to various wave frequency components and resonance modes, are grouped on the basis of electron energy and time. This method of grouping is chosen because the pitch-angle deflections for particles of a certain energy that arrive at the ionosphere at a given time essentially belong to the same particle (or bunch of gyrotropic particles), regardless of where along the field the pitch-angle changes may have actually occurred. Secondly, we square and add equatorial (rms) pitch angle deflections because we assume that the pitch angle changes in any given latitude bin are not correlated with pitch angle changes occurring in any other latitude bin. This method can lead to errors if the pitch-angle scatterings in adjacent bins are indeed correlated.

[32] We show a typical $\Delta\alpha_{\text{eq}}$ plot in Figure 7 which demonstrates how a constant frequency wave at the mag-

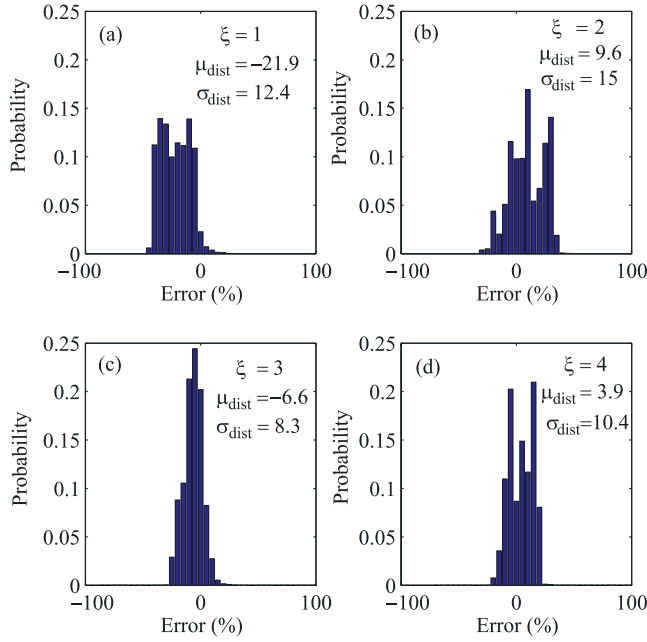


Figure 8. Latitude discretization error study for $L = 2.3$, $f \approx 3$ kHz showing the mean and variance for (a)–(d) 1° – 4° latitude windows.

netic equator interacts with a group of particles at the respective resonant energies at $L = 3$ and $L = 5$. Typical MR whistler parameters are chosen for this example from the $\lambda_s = 35^\circ$ simulation, with $f = 3$ kHz, θ near the Gendrin angle, and wave power of $\sim 2.5 \times 10^{-14}$ W/m²/Hz (which corresponds to ~ 0.3 pT with the chosen parameters at $L = 3$). In Figure 7a we show that for the interaction scenario involving no f -variation and very slow ω_H variation, the interaction length in latitude is still $\sim 3.54^\circ$, very similar to the value at $L = 3$, though the net pitch-angle change is ~ 10 times greater. In the typical simulations we perform, the interaction length is necessarily shorter because $\partial f / \partial \lambda$, $\partial k_z / \partial \lambda \neq 0$.

[33] To quantify the errors incurred due to latitude discretization, we compare the pitch-angle changes experienced by a group of particles with and without latitude discretization. For this purpose we chose a typical L -shell ($L = 2.3$) and frequency band ($f \approx 3.2 - 3.3$ kHz) and use a large number ($\sim 26,500$) of combinations of typical wave parameters taken from the $\lambda_s = 35^\circ$ injection wave simulation (where λ_s is the source latitude of the causative lightning strike). The wave parameters were recorded at 1° latitude bins in the range $\lambda_i \approx -30^\circ$ to 40° . The wave parameters strictly apply to only the 1° interval, but for the purpose of our error study we extrapolate these parameters over a 10° latitude range, spanning $\pm 5^\circ$ about each λ_i . We then integrate (3) for the resonant particles to obtain the pitch angle change $\Delta\alpha_{i0}$ for the particular 10° latitude span centered at λ_i . To measure how well discretization compares with the nominal pitch angle change $\Delta\alpha_{i0}$, we further subdivide the 10° latitude interval into ten 1° subintervals, integrate (3) in each subinterval to obtain the partial pitch angle changes ($\Delta\alpha_{i1}$ to $\Delta\alpha_{i10}$), compute $(\Delta\alpha_{i1}^2 + \dots + \Delta\alpha_{i10}^2)^{1/2}$ and compare to $\Delta\alpha_{i0}$.

[34] To go a step further, we introduced a ‘windowing’ operation, whereby the windowed partial pitch angle changes $\Delta\alpha_{i1\xi} - \Delta\alpha_{i10\xi}$ are evaluated over an interval of $\xi\Delta\lambda$, and the quantity $\left[\frac{1}{\xi}(\Delta\alpha_{i1\xi}^2 + \dots + \Delta\alpha_{i10\xi}^2)\right]^{1/2}$ is calculated as before. We would expect that as $\xi \rightarrow 10$, the error would tend to 0, and this is indeed the case. We show the results of our error study for $\xi = 1, 2, 3$, and 4 in Figure 8, where the distributions are obtained by adding the value $\Delta\alpha_{i0}$ into the appropriate error bin and then normalizing, and errors span from -100% to 100% divided into 5% bins. The choice of adding $\Delta\alpha_{i0}$ into the appropriate error bin as opposed to simply incrementing a counter in that bin was made because not all errors are equally significant. The change in pitch angle spans many orders of magnitude $\approx 10^{-15}$ – 10^{-1} and often the largest errors occur at the smallest $\Delta\alpha_{i0}$ ’s (in the nulls shown in Figure 6c and discussed above) where the pitch-angle change is well within the numerical noise level.

[35] As shown in Figure 8 the discretized results agree reasonably well with the non-discretized results (bearing in mind the huge scale variations of the $\Delta\alpha_{i0}$ ’s mentioned above). As ξ increases the mean of the distribution μ_{dist} tends to zero fairly quickly, but the standard deviation σ_{dist} does not, remaining at $\sim 10^\circ$ (the distribution does become narrower, but this is only visible for larger values of ξ). In the remainder of this paper we use a sliding ‘window’ of 2° (but still spaced at every 1°) because in general we obtain the largest differential improvement in mean value in changing from $\xi = 1$ to $\xi = 2$, and a marginal increase in σ_{dist} (we expect that as the sample size increases, σ_{dist} would become slightly smaller in the latter case). Although further improvements may come about with higher values of ξ , we have chosen not to make the integration window larger because the windowing operation results in a convolution or ‘smearing’ in time. Electrons scattered in an interaction occurring at a certain λ_i arrive at the ionosphere with a time-uncertainty corresponding to the flight time of the particle through the ξ° latitude interval. For instance, a 10 keV particle at the loss-cone has a time-uncertainty of ~ 0.02 sec at $L \approx 5$ and ~ 0.01 sec at $L \approx 2.3$. Since our $E - t$ plots have a time resolution (Δt) of 0.02 sec we have chosen not to use higher values of ξ so as to not make the time-smearing greater than Δt .

[36] To summarize our major tradeoffs, we note that wave parameters were calculated at 1° latitude intervals since this is the coarsest latitude sampling allowable, which would nevertheless ensure that wave power traveled approximately one time-bin (or less) in the spectrogram between adjacent latitude bins for typical wave parameters. Using the 1° latitude sampling for the wave parameters, we chose to integrate the test-particle equation (3) with a 2° window which is the largest integration interval possible, which nevertheless ensures a time-spread in the precipitated ionospheric flux of approximately one time-bin (or less) for typical test-particle parameters. Using the above discretization scheme gives errors of $\mu_{\text{dist}} \approx 10^\circ$, $\sigma_{\text{dist}} \approx 15^\circ$ when compared to scattering by constant frequency tones at $L = 2.3$, which is considered to be representative of the discretization errors expected over the whole simulation space. This is due to the self-similarity of MR whistlers when

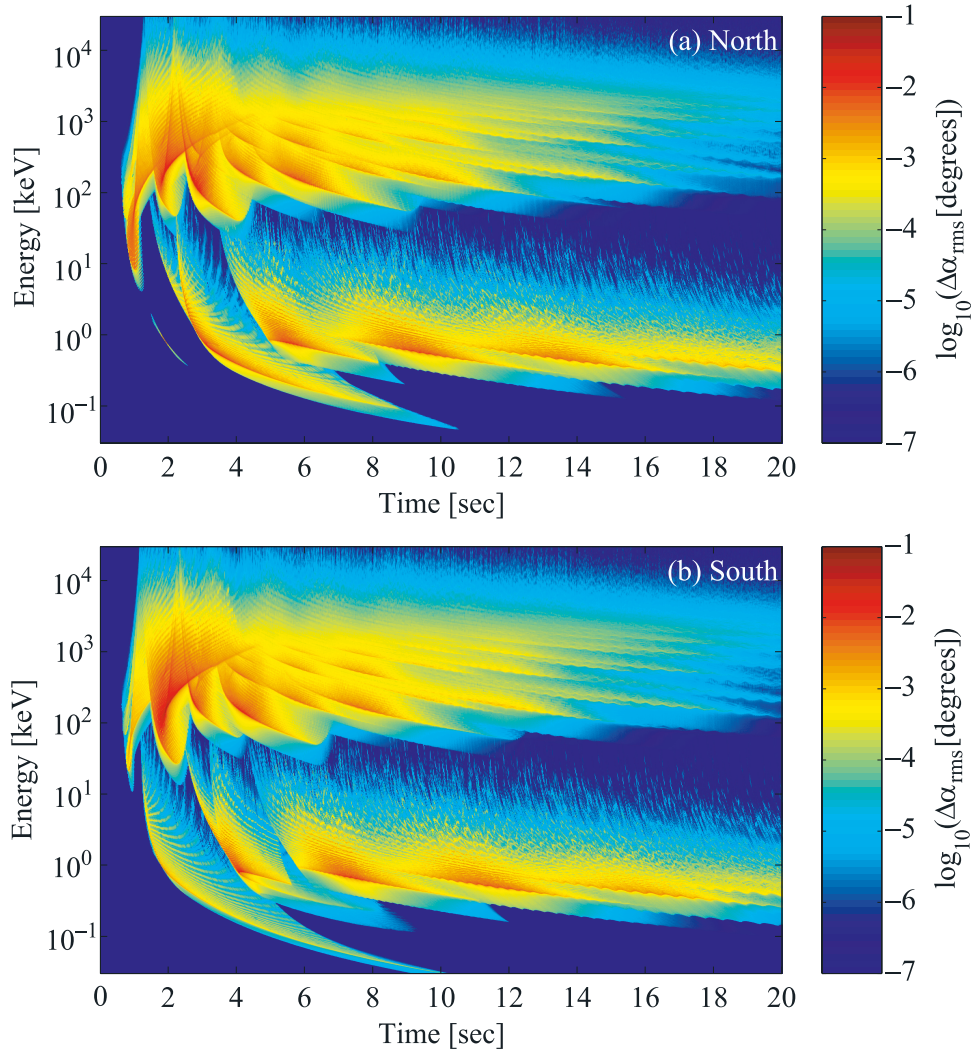


Figure 9. The pitch-angle deflection array as a function of particle energy E and arrival time at the ionosphere t , for a lightning source latitude of $\lambda_s = 35^\circ$, and observed at $L \simeq 3$.

normalized by the equatorial gyrofrequency [Lundin and Krafft, 2001], which is how resonant electrons naturally tend to perceive the wave from (1).

[37] In the error study discussed in Figure 8 above, we have assumed a constant frequency over the entire 10° latitude interval which gives the somewhat pessimistic error estimates near the equator. However, when simulating off-equatorial cases $\partial f/\partial\lambda = 0$ but $\partial\omega_H/\partial\lambda \neq 0$ which can also be interpreted as an equatorial interaction (i.e., $\partial\omega_H/\partial\lambda = 0$) with a varying frequency tone $\partial f/\partial\lambda \neq 0$. Since we sample both sides of the equator (i.e. $\partial\omega_H/\partial\lambda > 0$ and $\partial\omega_H/\partial\lambda < 0$) we effectively capture signals whose frequency both increases and decreases as a function of time.

[38] A final point to note about Figure 8 is that the $f - t$ slope of whistlers does indeed tend to decrease after several bounces of the wave, causing the tone to appear more constant and thus increasing the interaction length [Bortnik et al., 2003b]. However, real measured spectrograms show that the tones also become more incoherent and noisy (Figure 1), which makes the wave-particle interactions more diffusive rather than coherent. While we cannot

quantify the error associated with this effect directly, we do again point out that our approach is naturally suited to model this loss of coherence. Since the typical variation of the outer radiation-belt fluxes (which are the available population for scattering) can be a factor of ~ 100 during disturbed conditions, our bound on the discretization error seems quite acceptable.

[39] Figure 9 shows a typical equatorial pitch-angle deflection array, calculated as described above, displayed as a function of particle energy E , and arrival time at the ionosphere t for both northern (Figure 9a) and southern (Figure 9b) hemispheres at the ionospheric endpoints of the $L \simeq 3$ field-line. The most intense pitch-angle scattering is associated with the first ($m = 1$) counterstreaming cyclotron resonant interaction between energetic particles and the first few hops of the MR whistler wave. Peak deflections are $\sim 0.1^\circ$ occurring between ~ 100 keV and ~ 1 MeV. This pitch-angle deflection array corresponds to the precipitated differential number flux shown in Figures 13c and 13d, where a more complete discussion of the detailed $E - t$ features is given.

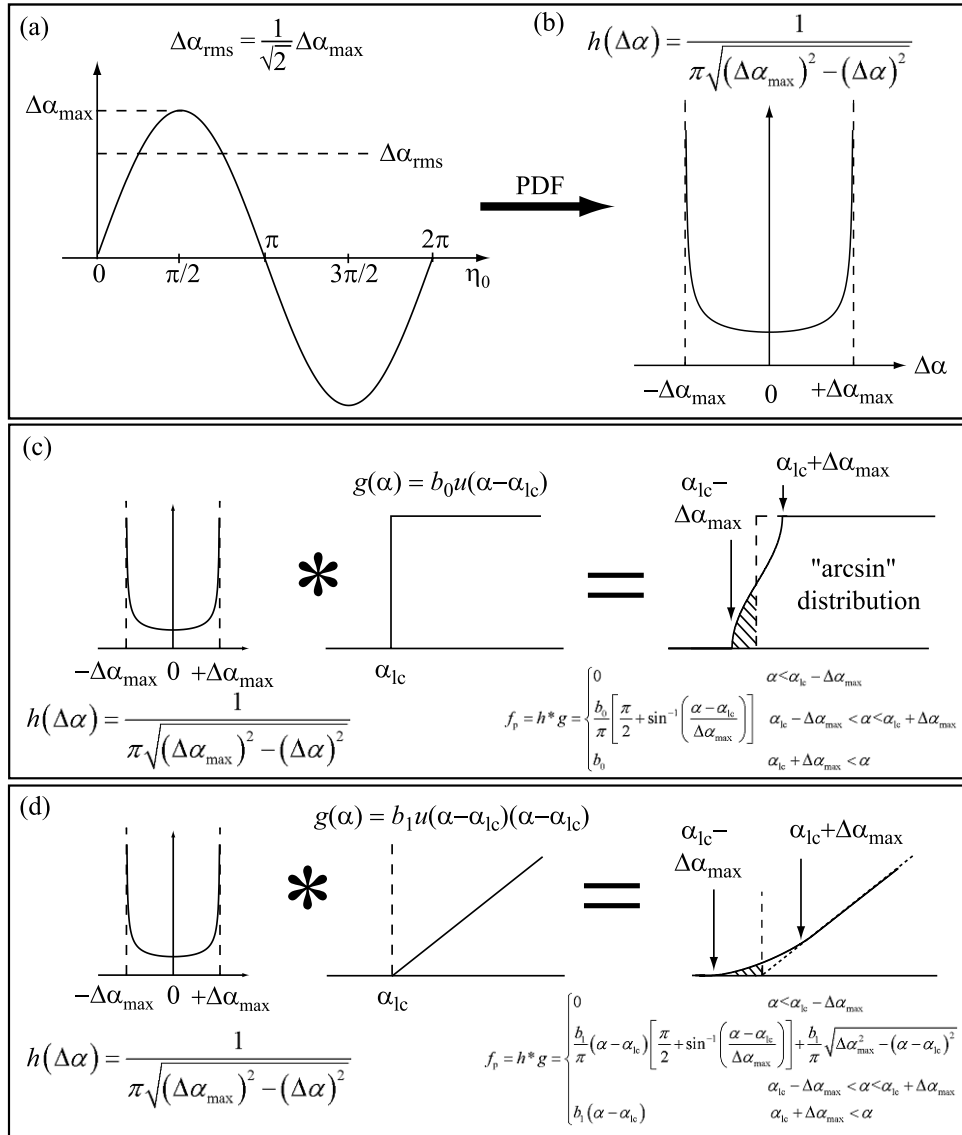


Figure 10. Analytic determination of precipitated flux (a) equatorial pitch-angle change as a function of initial angle (b) PDF of (a), (c) convolution of ‘sine’ scattering with square distribution, and (d) convolution of ‘sine’ scattering with a ramp function.

2.3. Determination of the Precipitated Flux

[40] After carrying out the above procedure as illustrated in Figure 4 over every $f - t$ bin at every latitude location, and for all resonance modes, we are left with two tables (one each for the northern and southern ‘feet’ of the field line) whose entries represent the total equatorial pitch-angle variances $\langle (\Delta\alpha_{\text{rms}})^2 \rangle$ of the perturbed particle distributions as a function of particle energy and ionospheric arrival times, shown in Figure 9. In order to obtain results that can be compared with measurement, we need to transform the pitch-angle change table into a corresponding table of precipitated flux. In past work [Inan *et al.*, 1978; Chang and Inan, 1985b; Jasna, 1993; Lauben *et al.*, 2001], this transformation has been implemented with an algorithm that mapped an unperturbed distribution in velocity-pitch-angle space into the perturbed distribution by applying the calculated pitch angle perturbation to each individual test-particle, and then using the distribution function to

determine the total flux of particles that has scattered into the loss-cone. Based on the relatively insensitive dependence of scattering on the initial pitch-angles, portions of the distribution function immediately above the loss cone were perturbed with the same set of values as the population at the edge of the loss cone, allowing the determination of all particles that could possibly be scattered.

[41] The procedure outlined above can be summarized with the following steps, and illustrated in Figures 10a and 10b:

[42] 1. Calculate a ‘perturbing function’ (e.g., Figure 10b that corresponds to the sinusoidal scattering shown in Figure 10a) that describes how a group of particles with the same pitch-angle and energy is scattered in pitch-angle as a function of initial phase η_0 .

[43] 2. Multiply the perturbing function with the value of the distribution function at the loss-cone.

[44] 3. Shift perturbing function to slightly higher pitch-angle and multiply with the new value of the distribution

function. Continue shifting the perturbing function and multiplying (scaling) by the value of the distribution function.

[45] 4. Integrate all the shifted-and-scaled replicas of the perturbing function to obtain the new ‘disturbed’ distribution function, i.e., the distribution function after the wave has scattered a portion of the particles into the loss-cone.

[46] This operation essentially amounts to numerical convolution, and since we have a deterministic scattering function h (Figures 10a and 10b) and deterministic distribution function g , the convolution can be performed analytically thereby reducing computation time.

[47] The convolution operation is illustrated in Figures 10c and 10d. In Figure 10c, we convolve a ‘square’ pitch angle distribution (a uniform distribution in pitch angle, with a sharp cutoff at the loss-cone) of magnitude b_0 with a scattering function characterized by the maximum pitch-angle change $\Delta\alpha_{\max}$. The analytical result of the convolution is shown in Figure 10c, and is given as:

$$f_p = h * g = \begin{cases} 0 & \alpha < \alpha_{lc} - \Delta\alpha_{\max} \\ \frac{b_0}{\pi} \left[\frac{\pi}{2} + \sin^{-1} \left(\frac{\alpha - \alpha_{lc}}{\Delta\alpha_{\max}} \right) \right] & \alpha_{lc} - \Delta\alpha_{\max} < \alpha < \alpha_{lc} + \Delta\alpha_{\max} \\ \frac{b_0}{\pi} & \alpha_{lc} + \Delta\alpha_{\max} < \alpha \end{cases} \quad (15)$$

[48] In Figure 10d we show a similar result, derived for a ‘ramp’ distribution with the convolution result again shown in the panel, and given as:

$$f_p = h * g = \begin{cases} 0 & \alpha < \alpha_{lc} - \Delta\alpha_{\max} \\ \frac{b_1}{\pi} (\alpha - \alpha_{lc}) \left[\frac{\pi}{2} + \sin^{-1} \left(\frac{\alpha - \alpha_{lc}}{\Delta\alpha_{\max}} \right) \right] + \frac{b_1}{\pi} \sqrt{\Delta\alpha_{\max}^2 - (\alpha - \alpha_{lc})^2} & \alpha_{lc} - \Delta\alpha_{\max} < \alpha < \alpha_{lc} + \Delta\alpha_{\max} \\ \frac{b_1}{\pi} (\alpha - \alpha_{lc}) & \alpha_{lc} + \Delta\alpha_{\max} < \alpha \end{cases} \quad (16)$$

where $h = (\pi \sqrt{(\Delta\alpha_{\max})^2 - (\Delta\alpha)^2})^{-1}$ is the perturbing function in both cases. The loss-cone distribution function is given by $g = b_0 u(\alpha - \alpha_{lc})$ and $g = b_1 u(\alpha - \alpha_{lc})(\alpha - \alpha_{lc})$ in Figures 10c and 10d, respectively, where u is the step function, and the constants b_0 , b_1 are obtained from the trapped flux model (see following section). The convolution method can be applied to a distribution function p of arbitrary shape, by letting $g(\alpha) = bu(\alpha - \alpha_{lc})p(\alpha - \alpha_{lc})$ and expanding p into a Taylor series about α_{lc} . The first two terms are shown in Figures 10c and 10d, respectively, and higher order terms can be readily obtained (A7).

[49] The hatched areas of Figures 10c and 10d represent those particles scattered into the loss-cone. Our task now is to obtain the total precipitated flux, and to this end, we convert the perturbed distribution function $f_p(E, t, \alpha)$ into a perturbed flux function $\Phi_p(E, t, \alpha)$ using the following formula [Chang, 1983]:

$$\Phi_p(E, t, \alpha) = \frac{f_p(E, t, \alpha)v^2}{m\gamma^3} \quad (17)$$

[50] In order to obtain the differential precipitated flux, we multiply with a $\cos \alpha$ factor to obtain flux parallel to \mathbf{B}_0 , integrate Φ_p over the solid angle representing the loss-cone, and finally multiply the result obtained above by a factor $g_c =$

$(\sin^2 \alpha_{lc}^{\text{eq}})^{-1}$ representing the contraction in cross-section of the geomagnetic flux tube as particles travel from the equator to ionospheric altitudes [Lauben *et al.*, 2001]. This can be written as:

$$\begin{aligned} \Phi(E, t) &= \overbrace{\frac{1}{\sin^2 \alpha_{lc}}}^{\text{flux tube contraction}} \int_0^{2\pi} \int_0^{\alpha_{lc}} \Phi_p(E, t, \alpha) \underbrace{\cos \alpha}_{\text{adjustment for area } \perp \text{ to } \mathbf{B}_0} \underbrace{\sin \alpha d\alpha d\phi}_{\text{solid angle } d\Omega} \\ &= \frac{\pi}{\sin^2 \alpha_{lc}} \int_0^{\alpha_{lc}} \Phi_p(E, t, \alpha) \sin 2\alpha d\alpha \end{aligned} \quad (18)$$

where all values of α are taken to be equatorial, and ϕ is the azimuthal angle.

[51] Finally, the number of precipitating electrons $N(t)$ and the associated energy flux $Q(t)$ which they represent are found by integrating $\Phi(E, t)$ with respect to energy as:

$$N(t) = \int_{E > E_{th}} \Phi(E, t) dE \quad (19a)$$

$$Q(t) = \int_{E > E_{th}} E \Phi(E, t) dE \quad (19b)$$

respectively, where we integrate above the lower energy threshold E_{th} to facilitate comparison with particle detector measurements made for energies above some sensitivity threshold.

2.4. Modeling of the Trapped Particle Distribution

[52] We use two different models of the available flux of energetic radiation-belt particles: the extrapolated analytic function of Bell *et al.* [2002] with an assumed square loss-cone distribution, and the AE8 MAX radiation belt-model [Vette, 1991] with an assumed sinusoidal loss-cone distribution shown in Figure 11. We note that the ordinate label $J(E)$ is the integral over pitch-angle of the flux function Φ (17) (before it is perturbed by the wave) divided by 4π . These distributions were selected (1) to compare our work with similar past work, (2) to compare the precipitation signatures at different L -shells using a simple analytic function, and (3) to simulate a more realistic L -dependent particle population with a softer loss-cone distribution. Past workers [Inan *et al.*, 1978; Chang and Inan, 1985b; Jasna, 1993; Lauben *et al.*, 2001] have relied on the flux measurements taken by OGO 3 [Schield and Frank, 1970] for modeling the trapped energetic particle population, and quantitative comparison with past workers requires that we use the same distribution. On the other hand, the OGO 3 measurements were obtained in the region $4.2 < L < 5.7$, rely on a relatively small sample of observations, and are atypical in that they represent more intense fluxes (particularly in the suprathermal range) compared to more recent observations made aboard the POLAR satellite [Bell *et al.*, 2002], which were taken in the region $2.3 < L < 4$, and rely on the large HYDRA data set (see Figure 11). In this connection, it should be noted that we also use the POLAR fluxes in our evaluation of the Landau damping of the whistler-mode rays. In past work the determination of the trapped fluxes for higher energy electrons (>10 keV) were

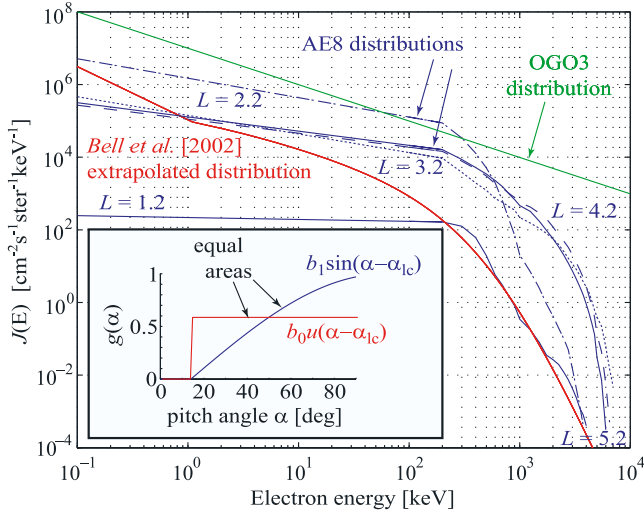


Figure 11. Energetic electron fluxes calculated using the AE8 model (blue curves) at $L = 2.2, 3.2, 4.2,$ and $5.2,$ and the extrapolated analytical distribution of *Bell et al.* [2002] (red curve) derived from HYDRA data. The inset shows the ‘sine’ and ‘square’ pitch-angle distributions associated with the AE8 and analytical distributions, respectively.

based on crude assumptions of E^{-n} type of scaling from OGO 3 measurements at ~ 1 keV of $f(v)$ with n ranging from 2 to 6. In our work, the distribution of higher (>10 keV) energy electrons is modeled in a manner consistent with HYDRA measurements of lower (<20 keV) energy electrons in that we extrapolate the distribution function of *Bell et al.* [2002] by modifying the particle velocity with the Lorentz factor, giving the expression:

$$f(v) = \frac{a_1}{v_m^4} - \frac{a_2}{v_m^5} + \frac{a_3}{v_m^6} \quad (20)$$

where f is in s^3cm^{-6} , v_m is the modified velocity given by $v_m = v/\sqrt{1 - v^2/c^2}$ where v is the velocity in $\text{cm}\cdot\text{s}^{-1}$, and $a_1, a_2,$ and a_3 are model constants set to $4.9 \times 10^5 \text{ cm}^{-2}\text{s}^{-1}$, $8.3 \times 10^{14} \text{ cm}^{-1}\text{s}^{-2}$, and $5.4 \times 10^{23} \text{ s}^{-3}$, respectively. This extrapolated distribution is shown in Figure 11 and exhibits a rolloff with energy that is similar to typical (solar maximum) AE8 fluxes, but tends to underestimate such fluxes by as much as a factor of a few hundred in the few 100 keV to few MeV range.

[53] The simple analytical distribution function given above lacks certain features necessary when producing ‘global’ views of the MR whistler driven precipitation signatures. Firstly, the actual trapped energetic particle fluxes are clearly L -dependent, producing the well-known radiation belt zones (inner belt, outer belt, and slot region shown in Figures 11 and 12). Secondly, the energy spectrum not only scales with L -shell, but the energy e -folding factor is L -dependent. Finally, a unique feature in the present work is the increased duration of the precipitation signature, due to the relatively long-lived (~ 10 sec) MR whistler waves. Previously [*Inan et al.*, 1978; *Chang and Inan*, 1985; *Jasna*, 1993; *Lauben et al.*, 2001], it was assumed that only the first equatorial crossing of the whistler was important for wave-induced particle precipitation, and thus only the first

equatorial crossing was modeled, so that the resonant electrons would only experience one counter-streaming first-order gyroresonant interaction. It was thus plausible that a fresh particle population would enter the wave-packet with a sharp cutoff at the loss-cone, interact with the wave resulting in erosion of the near-loss-cone distribution and that the eroded loss-cone distribution would not be encountered again by the wave. In this work, we consider many harmonic resonance interactions and the MR whistlers endure for tens of seconds, providing ample time for the same population of particles to mirror many times between hemispheres. Our solution is to assume a simple equilibrium loss-cone distribution after *Walt et al.* [2002] of the form $\Phi(E, L, \alpha) = b_1 \sin(\alpha - \alpha_{lc})$ where $b_1 = b_1(E, L)$ is found by integrating out the pitch angle dependence and comparing to the predicted model fluxes $J(E, L)$. We thus assume that the flux removed by the MR whistler-wave is immediately replenished from higher pitch angles, such that the equilibrium distribution remains constant for the duration of the MR whistler driven precipitation event. Our assumed pitch-angle distribution is based on the most recent analytical AE model (AE5) which uses a sinusoidal distribution raised to some power m (where $m \sim 1$), which is itself quite realistic, being based upon decades of radiation-belt measurements [*Vette*, 1991]. The assumption that our equilibrium pitch-angle distribution remains constant even after an interaction with the MR whistler requires some elaboration: firstly, since MR whistlers are confined to the plasmasphere [*Edgar*, 1972; *Bortnik et al.*, 2003b], the ratio of plasma frequency to gyrofrequency remains greater than 10, in which case the pitch-angle diffusion coefficient increases with α [*Glauert and Horne*, 2005]. This means that the same whistler that scattered the original ‘near loss-cone’ electrons into the loss cone, is able to bring higher pitch-angle electrons with the same (or greater) efficiency down

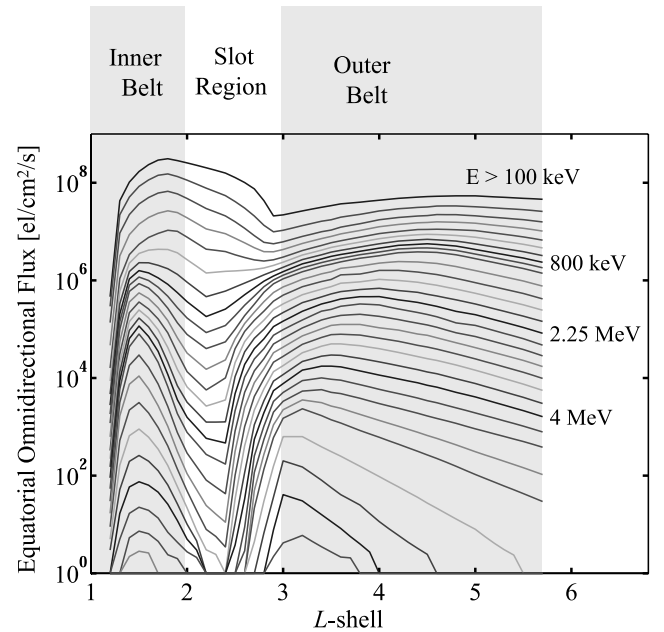


Figure 12. Equatorial omnidirectional flux of energetic radiation belt particles used in the computation of precipitated flux, calculated using AE8 model.

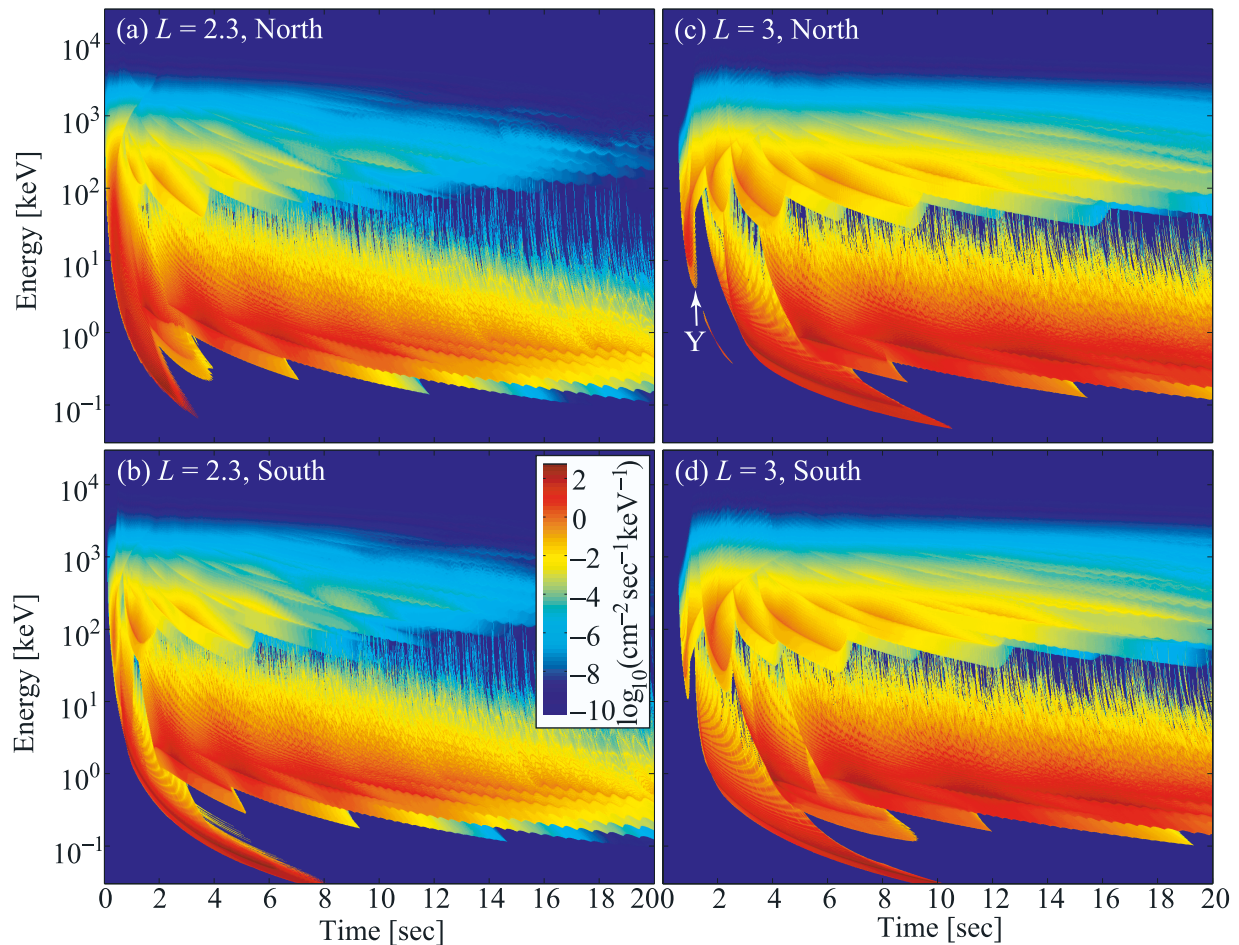


Figure 13. Precipitated differential number flux signatures at 100 km altitude, due to a lightning discharge at $\lambda_s = 35^\circ$ at $L = 2.3$ and $L = 3$ in the northern and southern hemispheres, with color-scale as shown.

to the loss cone and thus maintain the equilibrium distribution we assumed.

[54] In addition, the MR whistler drives a bunch of electrons into the loss-cone on a particular field-line, but this bunch is quite localized, especially in bounce phase. In effect, the pitch-angle distribution is degraded (if we assume no replenishing from higher pitch angles), but if the next reflection of the MR whistler wave interacts with a bunch of electrons on the same field line, it will very likely not match up to the exact bounce-phase of the previous bunch of electrons and thus effectively see an unperturbed pitch-angle distribution. A smaller effect is the eastward azimuthal drift (curvature and gradient drift) of fresh particle populations into the interaction region, thus again insuring that the wave always sees an equilibrium distribution.

[55] Finally, the loss-cone distribution is often not as soft as what we assumed, and can become a lot steeper [Inan *et al.*, 1989], driving far higher fluxes of precipitating electrons into the loss-cone. We thus believe that our estimate may be somewhat conservative.

[56] Analytically, this equilibrium pitch angle dependence is treated using a first order Taylor series expansion as shown in Figure 10d and Appendix A, which is a good approximation within a few degrees of the loss cone where

most of the precipitated flux originates. Using the AE8 model with the sinusoidal loss-cone distribution is expected to give realistic values of precipitation flux in the inner magnetosphere that are directly comparable to observations.

[57] The AE8 flux values are used only from the equatorial region, where $B/B_0 = 1$ (B is the local magnetic field line), and we assume the sinusoidal pitch-angle distribution described above such that the total pitch-angle integrated flux is maintained. In addition, the flux at values lower than ~ 100 keV is obtained by extrapolating the fluxes from >100 keV in log-space. As shown in Figure 11, these extrapolations intersect the measured 0.1–1 keV fluxes measured on POLAR, so we believe the extrapolations at intermediate energies are quite reasonable.

3. Simulation Results

3.1. Differential Number Flux

[58] The precipitated differential number flux signatures at the ionospheric end points (‘feet’) of two different field-lines are compared in Figure 13. The left and right columns show results for $L = 2.3$ and $L = 3$, and the top and bottom panels represent the northern and southern hemispheres,

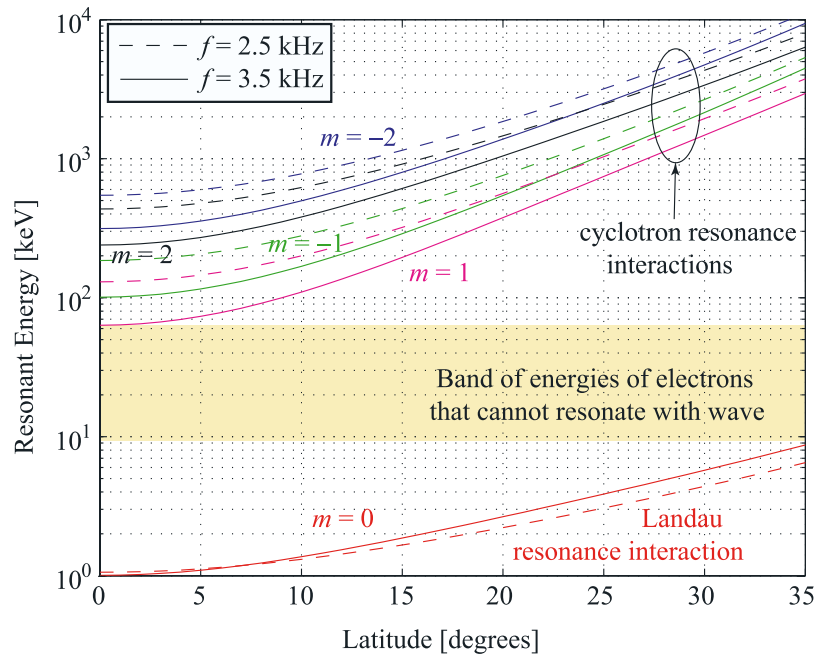


Figure 14. Resonant energies of electrons as a function of geomagnetic latitude at $L = 3$ for wave frequencies $f = 2.5$ kHz (dashed line) and $f = 3.5$ kHz (solid line), assuming $\theta = 80^\circ$, for harmonic resonances $m = -2$ to 2.

respectively. The energy is shown in keV on the ordinate, time in seconds on the abscissa, and differential number flux (where integration was performed in pitch-angle over the loss-cone as described in section 2.3) in electrons- $\text{cm}^{-2} \text{sec}^{-1} \text{keV}^{-1}$ on the color scale. The lightning source latitude was located at $\lambda_s = 35^\circ$, and we have used the extrapolated analytic function (20) with an assumed square loss-cone distribution for the trapped energetic particle flux.

[59] In examining Figure 13, certain common features are readily apparent in all the panels: there is a large band of precipitation between a few hundred eV and ~ 10 keV, peaking at ~ 1.5 keV. This intense flux is due to Landau resonance which scatters the lower energy particles into the loss cone. While the Landau resonance itself is less efficient than the ($m \neq 0$) gyroresonance modes, resulting in lower average pitch-angle changes, the abundance of lower energy particles compensates for this inefficiency, producing significantly higher number fluxes than other resonance modes.

[60] Near ~ 10 keV the Landau resonance flux decreases because the Landau resonance becomes less efficient, and an effective gap in the flux is created from ~ 10 keV up to a few tens of keV. The fact that Landau interactions occur with particles of energies up to ~ 10 keV comes about due to off-equatorial interactions at high wave-normal angles as discussed below and shown in Figure 14. The absence of precipitated flux in the energy band between ~ 10 keV and ~ 80 keV (for our typical lightning frequency spectrum) comes about due to the fundamental shift in the physical mechanism coupling particle and wave, from the Landau resonance to cyclotron resonance with no intermediate stages, and is indicated by the yellow band in Figure 14. The precipitated flux above ~ 80 keV is due to cyclotron

resonance of energetic particles with the wave. There are multiple ‘swaths’ of precipitation occurring at $E \gtrsim 80$ keV between 0 and ~ 6 sec in Figures 13a and 13b, and between 0 and ~ 14 sec in Figures 13c and 13d, resulting from the magnetospheric reflections (and thus multiple equatorial crossings) of the whistler wave packet. Since the wave-particle interaction is generally most efficient near the geomagnetic equator [Helliwell, 1967; Inan et al., 1983], these swaths appear discrete, descending in energy with time commensurate with the varying $f - t$ structure of the underlying wave, and to a lesser degree due the longer flight time to the ionosphere of lower energy particles from a particular wave-particle interaction location. The first gyroresonance ‘pulse’ in Figures 13a and 13b appears very broad in energy because the first hop of the whistler is wideband, containing frequency components from 200 Hz to 60 kHz, the majority of which (~ 8 –60 kHz) do not magnetospherically reflect and are absorbed in the ionosphere after the first equatorial traverse. These higher frequency components resonate with lower energy particles as is implied by (2), thus stretching the energy band of precipitated particles down to very low energies only in the first pulse. In the context of this discussion, it should be noted that the dependence of resonant energy on wave frequency is not simple, as it also involves the wave normal angle [through (2)], determined in the course of the computation of the ray path.

[61] A similar plot of differential number flux is shown in Figures 13c and 13d for $L = 3$. The same broad features are apparent in this plot: an intense band of low energy precipitating particles due to the Landau resonance, absence of precipitation at energies of a few tens of keV, and a higher energy component of multiple swaths of precipitating electrons due to the gyroresonant interactions.

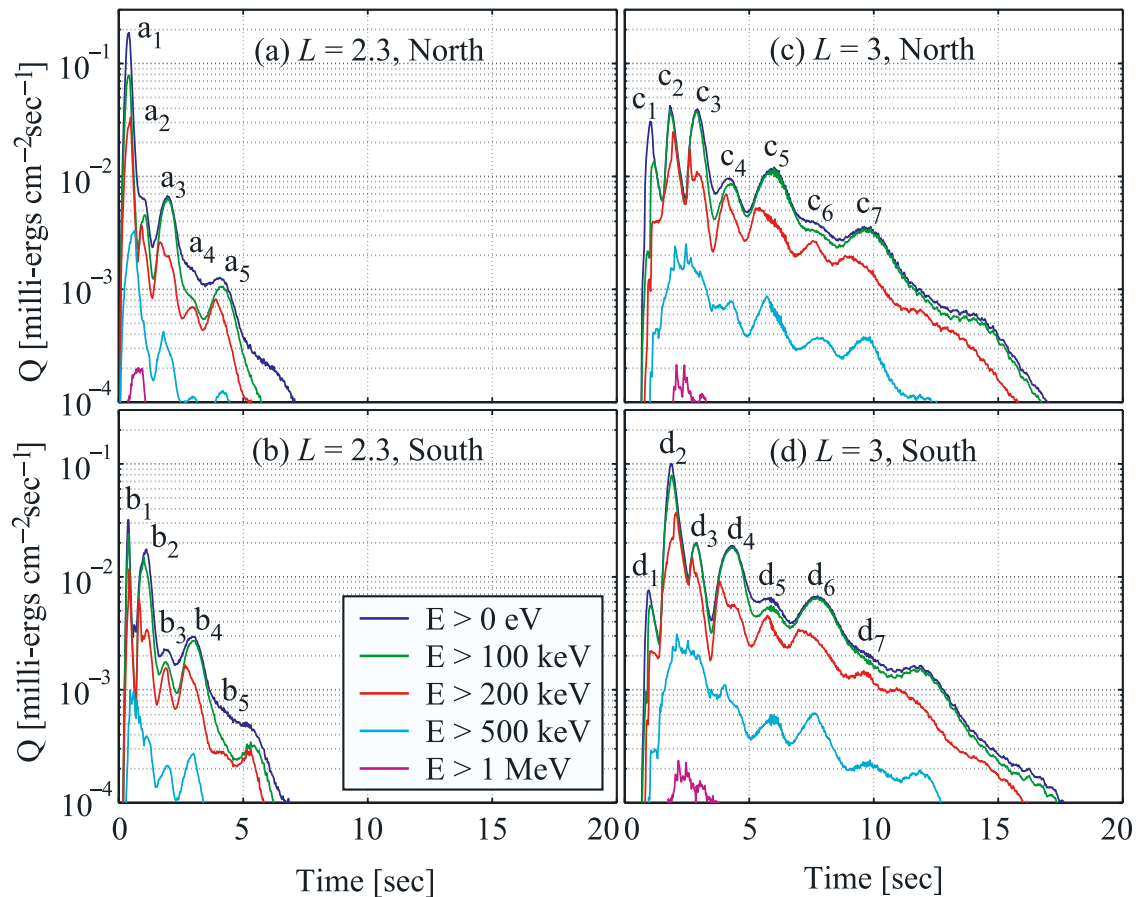


Figure 15. The precipitated differential number flux of Figure 13 integrated above various energy levels as indicated, giving energy flux. (a)–(d) Panels correspond to those in Figure 13.

[62] We illustrate the points discussed above by considering a simpler situation, shown in Figure 14 where the resonant energies of electrons are plotted as a function of geomagnetic latitude at $L = 3$ for two different wave frequencies $f = 2.5$ kHz (dashed line) and $f = 3.5$ kHz (solid line), a wave normal angle $\theta = 80^\circ$ and parametrized in harmonic resonance modes $m = -2$ to 2. We highlight in yellow the band of energies that do not resonate with the chosen wave frequencies over the latitude range shown, noting that they fall in a similar energy range ($E \simeq 10$ to 80 keV) to that in Figure 13. The resonant energy of particles increases with latitude for all resonance modes, and is typically higher for the lower frequencies for gyro-resonance ($m \neq 0$) wave-particle interactions.

[63] Returning now to Figure 13, a number of interesting and telling differences between the precipitation signatures at $L = 2.3$ and $L = 3$ are apparent. Firstly, the time of arrival of the first pulse at the ionosphere in both northern and southern hemispheres is significantly greater in Figures 13c and 13d than in Figures 13a and 13b implying a general motion of the precipitation footprint to higher latitudes with time, in agreement with the observations of Johnson *et al.* [1999] and consistent with the theoretical predications of Lauben *et al.* [2001]. The poleward motion of the precipitation footprint (due to the first hop of the whistler) with time is due to the longer distance (and hence longer time)

that whistlers must travel to illuminate higher L -shells compared with the lower L -shells, together with the increasing flight time (τ) of energetic electrons from equatorial regions to the ionosphere with L -shell. Our model results for the first hop of the oblique whistler have been compared with those of Lauben *et al.* [*Ibid*] for similar conditions, and excellent agreement has been found.

[64] Secondly, the duration of the event at $L = 3$ is longer than at $L = 2.3$, respectively requiring ~ 14 sec versus ~ 6 sec for the precipitation of the main portion of the gyroresonant flux. Lastly, note that the first precipitation pulse is narrower in energy in Figures 13c and 13d, compared to Figures 13a and 13b, since the majority of the injected whistler wave energy remains below $L = 3$ on its first equatorial traverse, does not MR, and is absorbed in the ionosphere thereafter.

[65] Other interesting features to note in Figure 13c are the “Y” structures (i.e., the apparent bifurcation of the first precipitated flux pulse, labelled “Y” on the figure) at $t \simeq 1$ sec, $E \simeq 100$ keV, reminiscent of those reported in Lauben [1999, p. 39]. These structures are caused by different frequency components (of a single wave packet) at different wave normal angles that interact with particles of the same energy but at different latitude locations on the field line, resulting in different arrival times at the ionosphere and the appearance of a ‘gap’ between the two limbs of the “Y-structure”.

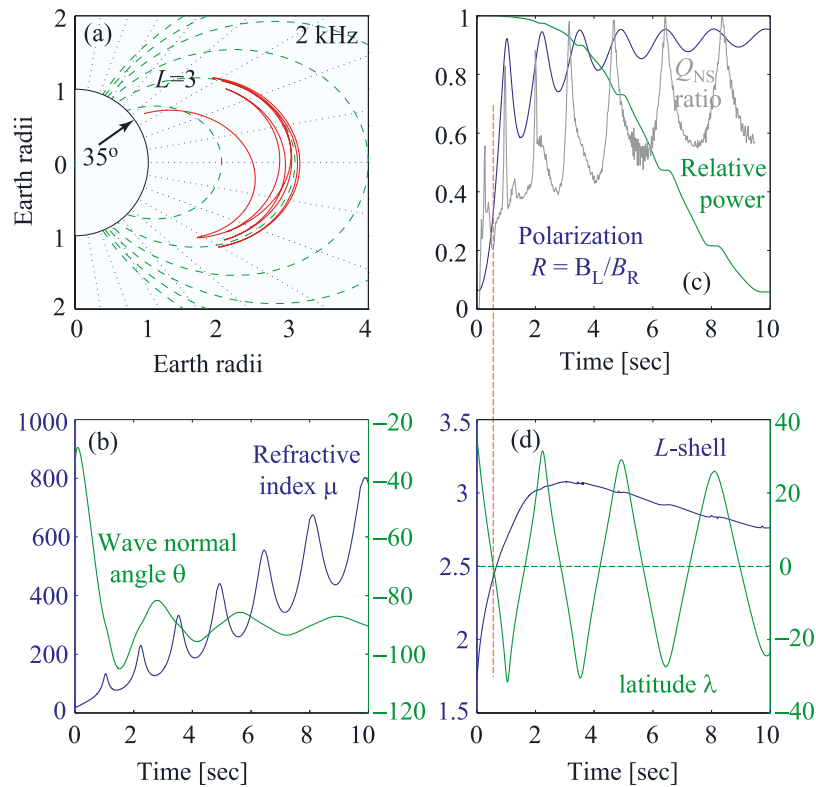


Figure 16. A 2 kHz ray showing (a) ray path, (b) refractive index and wave normal angle, (c) polarization ratio, relative power, and ratio of primary to secondary Q peaks (in Figure 15), and (d) L-shell and dipole latitude, for 10 sec of propagation.

[66] At $t \gtrsim 4$ sec, and $E \sim 700$ keV, Figures 13c and 13d show distinct ‘secondary’ swaths of precipitation, appearing fainter and at higher energies than the more intense primary swaths beneath them. These features are a result of second harmonic gyroresonance interactions ($m = 2$), also visible in Figure 9. At even higher energies, the higher order gyroresonance scattering merges into the diffuse drizzle of precipitating particles, and loses its discrete appearance. The secondary swaths are also visible in Figures 13a and 13b though not as clearly.

[67] We note that in Figure 13 some diagonal striations are visible in the top portion of the Landau precipitation flux at $E \sim 10$ keV. These are due to numerical noise related to the latitude discretization and are not a physical feature. As discussed in section 2.1, increasing the latitude sampling resolution (i.e., discretizing latitude in $<1^\circ$ bins) reduces the striations, resulting in the appearance of a smoother precipitation signature, but degrades the accuracy of the overall pitch-angle change calculation.

3.2. Energy Flux

[68] Using the information presented in Figure 13 we now calculate the precipitated energy fluxes $Q(t)$ shown in Figure 15, by integrating the differential number fluxes $\Phi_p(E, t)$ above various energy thresholds using (19b).

[69] This calculation is done to facilitate comparison with ground based measurements, since ionospheric effects (e.g., secondary ionization, optical emissions) are generally interpreted in terms of the precipitated energy flux. As discussed in section 3.1 in connection with Figure 13, the timing

differences between the two field-lines are readily apparent, the energy flux at $L = 3$ arriving later, and enduring longer than that at $L = 2.3$.

[70] By comparing the energy fluxes above various thresholds, we can infer the contributions of the different harmonic resonance modes to the total energy flux. For example, the energy flux curves >0 keV (blue) and >100 keV (green) show little difference, implying that the intense Landau precipitation fluxes visible in Figure 13 contain little energy and hence do not significantly contribute to ionospheric effects (the two curves differ in some places, but this is due to the lower energy gyroresonant particles). Using the same technique, it is evident that $\sim 80\%$ to 90% of the energy flux is composed of electrons in the range 100 keV to 500 keV, and $>99\%$ of the energy flux is composed of electrons <1 MeV. It should be noted, however, that ionospheric effects are also determined by the altitude of penetration of the electron into the ionosphere, which in turn is dependent on particle energy [Banks *et al.*, 1974]. For example, while >100 keV electrons deposit their energy at D-region altitudes or lower (<90 km), any significant perturbations at E- and F-region altitudes we generally be produced by tens of keV electrons.

[71] The curves shown in Figure 15 all exhibit a periodic structure which is attributed to the multiply reflecting nature of the whistler and the fact that interactions are most efficient near the geomagnetic equator. In Figure 15a, we note that alternate maxima are more intense (e.g., a_1, a_3, a_5), with the intervening maxima (a_2, a_4) being less intense, while in the conjugate hemisphere, this pattern is again

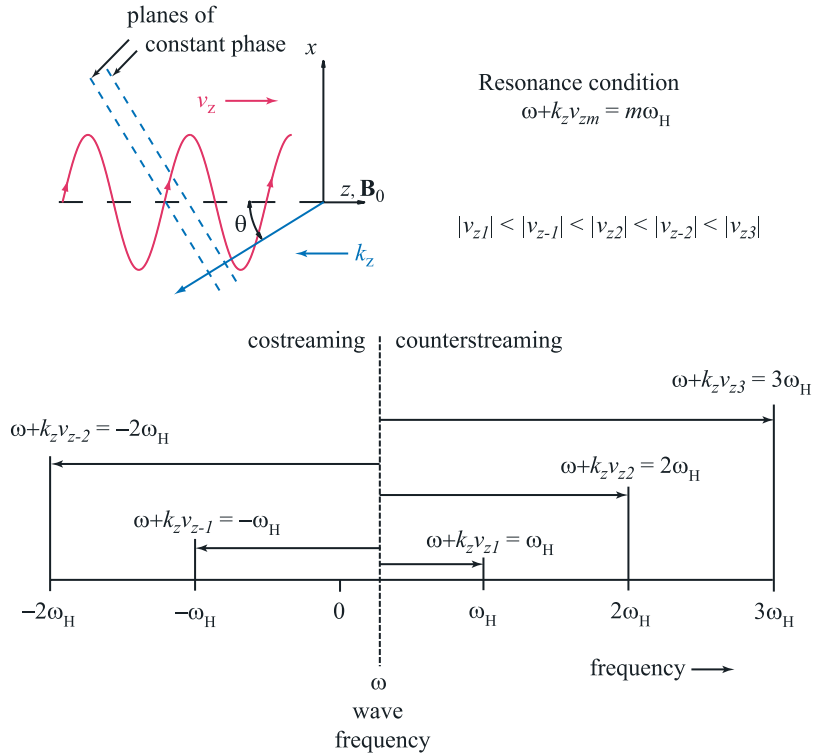


Figure 17. Qualitative illustration of the behavior of v_z for various resonance modes m for resonant wave-particle interactions.

evident but the primary (b_2, b_4) and secondary (b_1, b_3, b_5) maxima are now reversed relative to those in the northern hemisphere.

[72] The structure of alternating maxima can be understood by analyzing the propagation and characteristics of the whistler wave that drives the precipitation. In Figure 16 we plot a representative ray injected at 35° latitude, with a frequency of 2 kHz and examine the first 10 seconds of propagation. As can be seen from Figures 16a or 16d (blue curve), this frequency component illuminates the $L \simeq 3$ region, so we use it as a crude proxy for the wave packet, and use Figures 15c and 15d to compare wave and particle behavior at $L = 3$.

[73] We note in Figure 15 that the first pulse in the northern hemisphere (c_1) is larger than that in the southern hemisphere (d_1), which is similar to that at $L = 2.3$ where $a_1 > b_1$. The second pulse also shows the same trend in both L -shells with $b_2 > a_2$ and $d_2 > c_2$, but note that the magnitude of the precipitated energy flux in d_2 is significantly larger than c_1 , unlike that of $L = 2.3$. The reason for this can be inferred by examining Figure 16a, where the ray injected directly above the lightning discharge (and hence carrying most of the power) entirely misses $L = 3$ on its first hop, but illuminates it on its second hop causing the precipitation to be more intense. The first precipitation maxima c_1 and d_1 are caused by the first equatorial traverse of rays injected at higher latitudes ($\lambda > 35^\circ$) than our computed ray and hence carry less wave power since they are further from the source.

[74] The alternating energy flux maxima are attributed to the fact that the wave-particle interaction is always more effective in the counterstreaming direction. Hence, on the

first hop the wave travels south and the primary precipitation peak (c_1) is in the north. After ~ 1 sec, the wave experiences a magnetospheric reflection at $\lambda \simeq -30^\circ, L \simeq 2.6$ as shown in Figure 16d, and begins to travel north, resulting in a primary precipitation peak in the south (d_2).

[75] There are a number of reasons why counterstreaming interactions result in higher precipitated fluxes: firstly, according to the resonance condition, (1), when the wave and particle move in opposite directions, the Doppler shift resulting from the relative motion naturally raises the apparent wave frequency as shown in Figure 17 for v_{z1} , whereas for a particle moving in the same direction as the wave the Doppler shift lowers the apparent frequency v_{z-1} . For resonance in the counterstreaming mode, the particle only needs to raise the wave frequency to match a multiple of its gyrofrequency (v_{z1}, v_{z2} , or v_{z3}), whereas in the co-streaming interaction the particle velocity parallel to the ambient magnetic field must exceed the phase velocity of the wave until the apparent frequency is equal to a negative multiple of the particle's gyrofrequency (v_{z-1}, v_{z-2} , or v_{z-3}). The particle velocity required for counterstreaming gyroresonance is thus lower than that required for co-streaming gyroresonance, for the same absolute value of the resonance harmonic $|m|$ (because ω is assumed positive), and increases with m such that $|v_{z1}| < |v_{z-1}| < |v_{z2}| < |v_{z-2}| < |v_{z3}|$ and so on.

[76] Since available particle fluxes fall rapidly with energy (Figures 11 and 12), the energy flux of the counterstreaming particles is higher because of the relative abundance of the lower energy particles. For instance, referring to Figure 11 again, we see that at $L \simeq 2.2$, increasing the energy of resonant electrons from 100 keV to 1000 keV, results in a

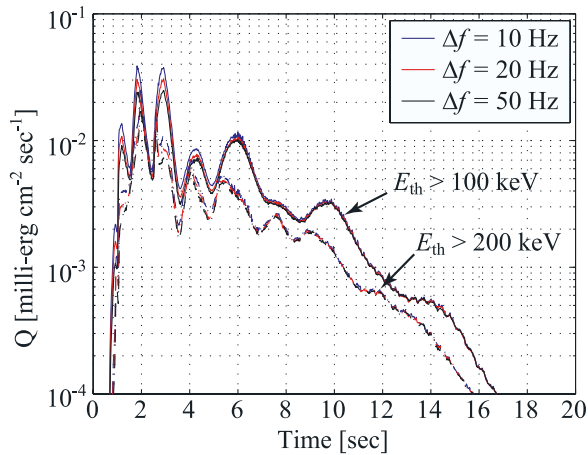


Figure 18. Sensitivity of the precipitated energy flux Q , to changes in the frequency bin size Δf . Solid and dashed lines correspond to energy thresholds of 100 keV and 200 keV, respectively.

decrease of the trapped flux by a factor of ~ 1000 , leading to an overall precipitated energy decrease of a factor of ~ 100 . This effect becomes less significant as ω/ω_H tends to zero.

[77] In addition to the points discussed above, the counterstreaming and co-streaming precipitated energy fluxes in the northern and southern hemispheres are asymmetric for yet another reason. In the development of the wave-particle interaction equations, we decompose the elliptically polarized oblique whistler wave, into left- and right-hand circularly polarized (LHCP and RHCP, where the latter is taken in the same sense of rotation about \mathbf{B}_0 as the electrons) components [Bell, 1984]. Since the electrons gyrate about the magnetic field line in a right-hand sense, they can only resonate with electromagnetic waves which are also “apparently” RHCP, and rotating at the same frequency. As we have discussed above, when the wave and electron approach each other (counterstreaming) the RHCP component of the wave is involved, and since $\omega < \omega_H$ for the whistler mode, its frequency is Doppler shifted to higher values to resonate with the particle. However, in the co-streaming mode the particle overtakes the wave, and in fact changes the apparent sense of rotation such that it is actually the LHCP component of the whistler that interacts with the electron, its left-hand polarization appearing as a right-handed rotation which matches the gyrofrequency of the electron. This realization leads to the question of the degree to which the relative magnitudes of the LHCP and RHCP control the north-south asymmetry of the precipitating energy flux.

[78] We address this question in Figure 16c, where we plot the ratio R of the wave’s LHCP magnetic field magnitude to the wave’s RHCP magnetic field magnitude (blue curve). Initially the ratio R is very low indicating that the wave is almost entirely RHCP (in fact, for parallel propagation $\mathbf{k} \parallel \mathbf{B}_0$, the whistler is strictly RHCP [Stix, 1992, p. 10]), and the wave normal angle θ in Figure 16c is $\lesssim 60^\circ$ near the geomagnetic equator on the first hop. However, R increases rapidly and within ~ 4 seconds becomes > 0.8 indicating that the LHCP and RHCP components are very close in magnitude. In order to compare the polarization

ratio R with the ratio of co-streaming versus counterstreaming precipitated fluxes, we show in Figure 16c the “ Q_{NS} -ratio” (grey), which is obtained by dividing the blue curve ($E > 0$ keV) of Figure 15c by the blue curve of Figure 15d, and inverting this ratio when it is > 1 , thus giving the ratio of the secondary flux maxima in one hemisphere to the primary flux maxima in the other hemisphere. The hemispherical energy flux ratio Q_{NS} curve was shifted back by 0.5 sec to roughly compensate for the electron flight time from the equator to the ionosphere.

[79] As shown in Figure 16c, at the first equatorial crossing of the wave (Figure 16d, green curve) the hemispherical energy flux ratio Q_{NS} and polarization ratio R are almost identical, but subsequent equatorial crossings indicate that Q_{NS} is much lower than R . We thus observe that the distribution of power among LHCP and RHCP wave components plays a smaller role in controlling the hemispheric precipitation asymmetry compared to the factors described above. The fact that the Q_{NS} and R are approximately equal on the first equatorial traverse is due to the fact that the wave packet contains a significant amount of power in the 8–60 kHz frequency range, and that the ray paths in this band do not experience magnetospheric reflections so that this effect is only evident on the first hop. These higher frequency components also resonate with electrons that are more separated in energy in the co-streaming and counterstreaming modes as implied by (1), and thus result in greater asymmetry in the precipitation and lower Q_{NS} due to the higher fluxes at lower energies.

[80] Before concluding our discussion of the precipitated energy flux, we briefly examine the sensitivity of the precipitated flux signature upon our choice of Δf , the bin size used in constructing the $f - t$ spectrograms which is used subsequently in the precipitation calculation. From (1), the bandwidth $\Delta\omega$ of a whistler wave that is able to resonate with an energetic particle over a resonance time Δt (where resonance time is defined as the time it takes the phase angle η to change by $\approx \pi$ during the course of the interaction) satisfies the condition $\Delta\omega\Delta t \approx 1$. Using typical parameters, e.g., $L = 3$, $E = 100$ keV, $\alpha_{LC} \approx 8.6^\circ$, and our assumed interaction length $\Delta\lambda = 2^\circ$, gives $\Delta f \approx 40$ Hz.

[81] In Figure 18 we repeat the calculation shown in Figure 15c, i.e., the precipitated energy flux in the northern hemisphere at $L = 3$, for $E_{th} > 100$ keV and $E_{th} > 200$ keV, using three different values of frequency bins, $\Delta f = 10, 20$, and 50 Hz. Results show that the flux values are relatively insensitive to Δf , varying far less than over the course of a typical simulation. The flux varies approximately as $1/\sqrt{\Delta f}$, particularly at the beginning of the simulation where there is a broad spectrum of waves resonating with a wide range of particle energies (resulting in a wide range of interaction times/lengths), but becomes far more uniform with time such as at $t = 6$ sec, the precipitated flux corresponding to $\Delta f = 10, 20$ and 50 Hz is very similar. As mentioned previously, in our work we choose $\Delta f = 10$ Hz, which is slightly smaller than the typical $\Delta f = 40$ Hz calculated above, but results in higher resolution $f - t$ spectrograms and hence better defined time-features, with resultant errors being less than a factor of 2 as shown in Figure 18.

[82] Having examined the details of the precipitated energy flux at two selected field-lines, we can repeat the calculation of precipitated flux over a range of field-lines spanning the entire inner magnetosphere from $L = 1.3$ to 5.5 in $0.1L$ increments, and examine the resulting ‘global’ view of the MR whistler driven precipitation event. This work and relevant discussion is the subject of a companion paper [Bortnik *et al.*, 2006].

4. Summary and Conclusions

[83] In this paper we presented a novel method to calculate (under equilibrium conditions) the differential number flux of precipitating energetic radiation-belt electrons due to an MR whistler wave initiated by a single cloud-ground lightning discharge. The precipitation flux is calculated at the northern and southern ‘feet’ of individual field-lines.

[84] We first calculate the $f-t$ spectra of the MR whistler wave as observed along a particular field-line at 1° latitude intervals. This is done by ray tracing ~ 5330 ray paths from the topside ionosphere, and interpolating between them to obtain ~ 120 million ray paths. Each ray path is weighted by an initial power at the topside ionosphere (which is latitude and frequency dependent), and the Landau damping is calculated along the ray path. An effective area is defined at a particular observing location, and the rays that traverse this area are recorded into a file, their wave power (and other wave characteristics) then being arranged according to frequency and time to produce simulated dynamic spectra. Further details and example spectrograms have been presented in a separate paper [Bortnik *et al.*, 2003b].

[85] We then use a novel technique to calculate the precipitated flux of energetic radiation belt electrons, which involves integration of the particle equations of motion (3) at 1° latitude bins, over 2° latitude windows. The pitch-angle changes are calculated over resonance modes $m = -5$ to 5 , as a function of energy and time, and are transformed to precipitated flux using a novel convolution technique, and the AE8 MAX trapped flux model with a realistic sinusoidal pitch-angle distribution as input. We have made numerous estimates of the errors involved in our calculations and conclude that the most serious errors are due to latitude discretization and are within $\sim 10\%$ of the case of a monochromatic wave with constant wave characteristics. Since MR whistlers have varying characteristics with space and time, this error estimate is considered quite conservative. We also compared our results with those of Lauben *et al.* [2001] using similar input conditions and neglecting magnetospheric reflections and Landau damping, and obtained excellent agreement (comparison not shown), again confirming the accuracy of the latitude discretization method used in the present work.

[86] We then simulated the precipitated flux of energetic electrons at the feet of the $L_1 = 2.3$ and $L_2 = 3$ field lines due to a 8.5 kA (peak) lightning discharge at $\lambda_s = 35^\circ$, and can draw the following conclusions:

[87] 1. The onset and duration times of the precipitated flux both increase with latitude in agreement with previous work [Lauben *et al.*, 2001].

[88] 2. There is an intense precipitation band below ~ 10 keV driven by the Landau resonance, which does not contribute significantly to the overall energy flux.

[89] 3. There is an energy gap in the precipitated flux between ~ 10 keV and ~ 80 keV due to a change in the coupling mechanism between the wave and the particle, from Landau resonance to gyroresonance.

[90] 4. Above ~ 80 keV the precipitation occurs in narrow energy ‘swaths’ which are discrete and result from the repeated traversals of the MR whistler wave energy across the magnetic equatorial plane, where wave-particle interactions are most efficient.

[91] 5. The resultant precipitated energy flux tends to be composed of a series of maxima, each maximum corresponding to an equatorial traversal of the MR whistler.

[92] 6. While electrons are scattered in pitch-angle in both costreaming and counterstreaming resonant interactions with the wave, it is always the counterstreaming interaction which results in the more intense fluxes, due to the slightly lower resonance energies and greater abundance of trapped particles (available for scattering) at those energies. The ratio of LHCP to RHCP wave energy in the elliptically polarized whistler seems to play a much smaller role in producing asymmetric fluxes.

[93] 7. Due to the particular propagation geometry of the MR whistler wave packet, the first maximum in the precipitated energy flux is not always the most intense, though this is generally the case.

[94] The methodology presented in this work is believed to be the first of its kind, allowing for a highly detailed characterization of the temporal, spatial, and spectral signatures of the precipitation of energetic electrons into the loss cone, including the effects of a range of gyroharmonic resonance modes ($m = -5$ to 5), multiple magnetospheric reflections, and wave power attenuation due to Landau damping. It has been verified with excellent agreement, through comparison with the work of Lauben *et al.* [2001] (i.e., when we use our model with the same initial conditions used by Lauben [1999]; not shown here), which has itself been tested experimentally [Johnson *et al.*, 1999]. As such, it constitutes a new and promising tool for the analysis of the impact of lightning and other VLF radiating structures (e.g., VLF transmitters or satellite-based transmitters) upon energetic electrons in the Earth’s radiation belts. Analysis of complete global signatures using our method for a variety of lightning discharge latitudes is given in a companion paper [Bortnik *et al.*, 2006].

Appendix A: Convolution Method of Calculating Pitch-Angle Scattering

[95] We consider a large number of test-particles entering the wave packet, and being scattered in pitch-angle as shown in Figure 10a. In this instance, the set of initial phase angles η_0 can be thought of as a random variable $\widehat{\eta}_0$ distributed uniformly in the interval $(0, 2\pi]$. Then $\Delta\alpha = \Delta\alpha_{\max}\sin(\widehat{\eta}_0)$ can be viewed as the sample of a sinusoidal waveform at random values of η_0 , that are uniformly distributed over the interval $(0, 2\pi]$. We now find the probability density function of $\Delta\alpha$.

[96] Using standard probability theory [see, e.g., *Leon-Garcia*, 1994, p. 126], we first find the cumulative distribution function $F_{\widehat{\Delta\alpha}}(\Delta\alpha)$:

$$\begin{aligned} F_{\widehat{\Delta\alpha}}(\Delta\alpha) &= P(\widehat{\Delta\alpha} \leq \Delta\alpha) \\ &= P(\Delta\alpha_{\max} \sin(\widehat{\eta}_0) \leq \Delta\alpha) \\ &= P\left(\widehat{\eta}_0 \leq \sin^{-1}\left(\frac{\Delta\alpha}{\Delta\alpha_{\max}}\right)\right) \\ &= \frac{1}{\pi} \left[\sin^{-1}\left(\frac{\Delta\alpha}{\Delta\alpha_{\max}}\right) + \frac{\pi}{2} \right] \end{aligned} \quad (\text{A1})$$

and then the probability density function $f_{\widehat{\Delta\alpha}}(\Delta\alpha)$ can be directly obtained:

$$f_{\widehat{\Delta\alpha}}(\Delta\alpha) = \frac{d}{d\Delta\alpha} F_{\widehat{\Delta\alpha}}(\Delta\alpha) = \frac{1}{\pi \sqrt{(\Delta\alpha_{\max})^2 - (\Delta\alpha)^2}} \quad (\text{A2})$$

where $|\Delta\alpha| \leq \Delta\alpha_{\max}$.

[97] To describe the perturbed distribution function we convolve the perturbing function (above), with the initial distribution function. Switching to the dummy variable $\tilde{\alpha}$ we let

$$h = \frac{1}{\pi \sqrt{(\Delta\alpha_{\max})^2 - (\tilde{\alpha})^2}} \quad (\text{A3})$$

and

$$g = u(\tilde{\alpha} - \alpha_{lc})p(\tilde{\alpha} - \alpha_{lc}) \quad (\text{A4})$$

where u is the step function, and p is an arbitrary function describing the distribution near the loss-cone. Then the perturbed function f_p is:

$$\begin{aligned} f_p(\alpha) &= h * g \\ &= \int_{-\infty}^{\infty} h(\tilde{\alpha}) * g(\alpha - \tilde{\alpha}) \\ &= \int_{-\infty}^{\infty} \frac{1}{\pi \sqrt{(\Delta\alpha_{\max})^2 - (\tilde{\alpha})^2}} u(\alpha - \tilde{\alpha} - \alpha_{lc}) p(\alpha - \tilde{\alpha} - \alpha_{lc}) d\tilde{\alpha} \\ &= \int_{-\Delta\alpha_{\max}}^{\alpha - \alpha_{lc}} \frac{1}{\pi \sqrt{(\Delta\alpha_{\max})^2 - (\tilde{\alpha})^2}} p(\alpha - \tilde{\alpha} - \alpha_{lc}) d\tilde{\alpha} \end{aligned} \quad (\text{A5})$$

[98] Now since $\Delta\alpha_{\max}$ is typically $\leq 1^\circ$, and often much smaller, we need only know the function p in the vicinity of α_{lc} . We can thus expand p using a Taylor series near 0 (MacLaurin series):

$$p(x) = \sum_{k=0}^{\infty} p^{(k)}(0) \frac{x^k}{k!} \quad (\text{A6})$$

where $p^{(k)}(0)$ denotes the k th derivative of p evaluated at $x = 0$. For example, when we expand p to zeroth order, $p(x) = b_0$, evaluation of (A5) gives the result (15). Expanding to first order, $p(x) = b_1x$, and evaluating (A5) gives the result (16). To expand p to a higher order, we

list the first few integral terms which are valid for $|x| \leq a$ for convenience:

$$\begin{aligned} \int \frac{1}{\sqrt{a^2 - x^2}} dx &= \sin^{-1}\left(\frac{x}{a}\right) \\ \int \frac{x}{\sqrt{a^2 - x^2}} dx &= -\sqrt{a^2 - x^2} \\ \int \frac{x^2}{\sqrt{a^2 - x^2}} dx &= -\frac{1}{2}x\sqrt{a^2 - x^2} + \frac{1}{2}a^2 \sin^{-1}\left(\frac{x}{a}\right) \\ \int \frac{x^3}{\sqrt{a^2 - x^2}} dx &= -\sqrt{a^2 - x^2} \left(\frac{2a^2}{3} + \frac{x^2}{3}\right) \\ \int \frac{x^4}{\sqrt{a^2 - x^2}} dx &= -\sqrt{a^2 - x^2} \left(\frac{3a^2x}{8} + \frac{x^3}{4}\right) + \frac{3}{8}a^4 \sin^{-1}\left(\frac{x}{a}\right) \\ \int \frac{x^5}{\sqrt{a^2 - x^2}} dx &= -\sqrt{a^2 - x^2} \left(\frac{8a^4}{15} + \frac{4a^2x^2}{15} + \frac{x^4}{5}\right) \end{aligned} \quad (\text{A7})$$

where the integrals are evaluated in the limits given by (A5), and linearly combined using the coefficients in (A6).

[99] **Acknowledgments.** This research was sponsored by the National Aeronautics and Space Administration (NASA) under grant NAG5-11821-0002, by the Air Force Office of Scientific Research (AFOSR) under grant F49620-03-1-0338, and also by NASA through subcontract via the University of Iowa under grant 4000083338-4 for the POLAR mission and under grant 4000061641 for the CLUSTER mission.

[100] Shadia Rifai Habbal thanks Reiner H. Friedel and Greg P. Ginat for their assistance in evaluating this paper.

References

- Abel, B., and R. M. Thorne (1998a), Electron scattering loss in Earth's inner magnetosphere: 1. Dominant physical processes, *J. Geophys. Res.*, *103*(A2), 2385–2396.
- Abel, B., and R. M. Thorne (1998b), Electron scattering loss in Earth's inner magnetosphere: 2. Sensitivity to model parameters, *J. Geophys. Res.*, *103*(A2), 2397–2407.
- Ashour-Abdalla, M. (1972), Amplification of whistler waves in the magnetosphere, *Planet. Space Sci.*, *20*, 639.
- Banks, P. M., C. R. Chappell, and A. F. Nagy (1974), A new model for the interaction of auroral electrons with the atmosphere: Spectral degradation, backscatter, optical emissions, and ionization, *J. Geophys. Res.*, *79*(10), 1459–1470.
- Bartels, J. (1936), The eccentric dipole approximating the Earth's magnetic field, *J. Geophys. Res.*, *41*, 225–250.
- Bell, T. F. (1984), Nonlinear gyroresonance interaction between energetic electrons and coherent VLF waves propagating at an arbitrary angle with respect to the Earth's magnetic field, *J. Geophys. Res.*, *89*(A2), 905–918.
- Bell, T. F. (1986), The wave magnetic field amplitude threshold for nonlinear trapping of energetic gyroresonant and Landau resonant electrons by conducted VLF waves in the magnetosphere, *J. Geophys. Res.*, *91*(A4), 4365–4379.
- Bell, T. F., U. S. Inan, J. Bortnik, and J. D. Scudder (2002), The Landau damping of magnetospherically reflected whistlers within the plasmasphere, *Geophys. Res. Lett.*, *29*(15), 1733, doi:10.1029/2002GL014752.
- Blake, J. B., U. S. Inan, M. Walt, T. F. Bell, J. Bortnik, D. L. Chenette, and H. J. Christian (2001), Lightning-induced energetic electron flux enhancements in the drift loss cone, *J. Geophys. Res.*, *106*(A12), 29,733–29,744.
- Bortnik, J. (2004), Precipitation of radiation belt electrons by lightning-generated magnetospherically reflecting whistler waves, thesis, Stanford Univ., Palo Alto, Calif.
- Bortnik, J., U. S. Inan, and T. F. Bell (2002a), L dependence of energetic electron precipitation driven by magnetospherically reflecting whistler waves, *J. Geophys. Res.*, *107*(A8), 1150, doi:10.1029/2001JA000303.
- Bortnik, J., U. S. Inan, and T. F. Bell (2002b), Temporal signatures of electron precipitation induced by magnetospherically reflecting whistlers, *Eos Trans. AGU*, *83*(47), Fall Meet. Suppl., Abstract SM52A-0558.
- Bortnik, J., U. S. Inan, and T. F. Bell (2003a), Energy distribution and lifetime of magnetospherically reflecting whistlers in the plasmasphere, *J. Geophys. Res.*, *108*(A5), 1199, doi:10.1029/2002JA009316.

- Bortnik, J., U. S. Inan, and T. F. Bell (2003b), Frequency-time spectra of magnetospherically reflecting whistlers in the plasmasphere, *J. Geophys. Res.*, *108*(A1), 1030, doi:10.1029/2002JA009387.
- Bortnik, J., U. S. Inan, and T. F. Bell (2006), Temporal signatures of radiation belt electron precipitation induced by lightning-generated MR whistler waves: 2. Global signatures, *J. Geophys. Res.*, *111*, A02205, doi:10.1029/2005JA011398.
- Carpenter, D. L., and R. R. Anderson (1992), An ISEE/whistler model of equatorial electron-density in the magnetosphere, *J. Geophys. Res.*, *97*(A2), 1097–1108.
- Chang, H. C. (1983), Cyclotron resonant scattering of energetic electrons by electromagnetic waves in the magnetosphere, *Tech. Rep. E414-1*, Stanford Univ., Palo Alto, Calif.
- Chang, H. C., and U. S. Inan (1983a), Quasi-relativistic electron-precipitation due to interactions with coherent VLF waves in the magnetosphere, *J. Geophys. Res.*, *88*(A1), 318–328.
- Chang, H. C., and U. S. Inan (1983b), A theoretical-model study of observed correlations between whistler mode waves and energetic electron-precipitation events in the magnetosphere, *J. Geophys. Res.*, *88*(A12), 53–58.
- Chang, H. C., and U. S. Inan (1985a), Lightning-induced electron-precipitation from the magnetosphere, *J. Geophys. Res.*, *90*(A2), 1531–1541.
- Chang, H. C., and U. S. Inan (1985b), Test particle modeling of wave-induced energetic electron-precipitation, *J. Geophys. Res.*, *90*(A7), 6409–6418.
- Chang, H. C., U. S. Inan, and T. F. Bell (1983), Energetic electron-precipitation due to gyroresonant interactions in the magnetosphere involving coherent-VLF waves with slowly varying frequency, *J. Geophys. Res.*, *88*(A9), 7037–7050.
- Clilverd, M. A., D. Nunn, S. J. Lev-Tov, U. S. Inan, R. L. Dowden, C. J. Rodger, and A. J. Smith (2002), Determining the size of lightning-induced electron precipitation patches, *J. Geophys. Res.*, *107*(A8), 1168, doi:10.1029/2001JA000301.
- Crary, J. H. (1961), The effect of the Earth-ionosphere waveguide on whistlers, *Tech. Rep. 9*, Stanford Univ., Palo Alto, Calif.
- Das, A. C. (1971), A mechanism for VLF emissions, *J. Geophys. Res.*, *76*, 6915.
- Edgar, B. C. (1972), The structure of the magnetosphere as deduced from magnetospherically reflected whistlers, *Tech. Rep. 3438-2*, Stanford Univ., Palo Alto, Calif.
- Glauert, S. A., and R. B. Horne (2005), Calculation of pitch angle and energy diffusion coefficient with the PADIE code, *J. Geophys. Res.*, *110*, A04206, doi:10.1029/2004JA010851.
- Helliwell, R. A. (1965), *Whistlers and Related Ionospheric Phenomena*, Stanford Univ. Press, Stanford, Calif.
- Helliwell, R. A. (1967), A theory of discrete VLF emissions from the magnetosphere, *J. Geophys. Res.*, *72*(19), 4773–4790.
- Inan, U. S. (1977), Non-linear gyroresonant interactions of energetic particles and coherent VLF waves in the magnetosphere, *Tech. Rep. 3414-3*, Stanford Univ., Palo Alto, Calif.
- Inan, U. S., T. F. Bell, and R. A. Helliwell (1978), Nonlinear pitch-angle scattering of energetic electrons by coherent VLF waves in the magnetosphere, *J. Geophys. Res.*, *82*(19), 127–142.
- Inan, U. S., T. F. Bell, and H. C. Chang (1982), Particle-precipitation induced by short-duration VLF waves in the magnetosphere, *J. Geophys. Res.*, *87*(A8), 6243–6264.
- Inan, U. S., R. A. Helliwell, and W. S. Kurth (1983), Terrestrial versus Jovian VLF chorus: A comparative study, *J. Geophys. Res.*, *88*(A8), 6171–6180.
- Inan, U. S., H. C. Chang, R. A. Helliwell, W. L. Imhof, J. B. Reagan, and M. Walt (1985), Precipitation of radiation belt electrons by man-made waves: A comparison between theory and measurement, *J. Geophys. Res.*, *90*(A1), 359–369.
- Inan, U. S., M. Walt, H. D. Voss, and W. L. Imhof (1989), Energy spectra and pitch angle distributions of lightning-induced electron precipitation: Analysis of an event observed on the S81-1 (SEEP) satellite, *J. Geophys. Res.*, *94*(A2), 1379–1401.
- Jasna, D. (1993), Gyroresonant scattering of radiation belt electrons by oblique whistler waves, thesis, Stanford Univ., Palo Alto, Calif.
- Jasna, D., U. S. Inan, and T. F. Bell (1992), Precipitation of suprathermal (100 eV) electrons by oblique whistler waves, *Geophys. Res. Lett.*, *19*(16), 1639–1642.
- Johnson, M. P., U. S. Inan, and D. S. Lauben (1999), Subionospheric VLF signatures of oblique (nonducted) whistler-induced precipitation, *Geophys. Res. Lett.*, *26*(23), 3569–3572.
- Kimura, I. (1966), Effects of ions on whistler-mode ray tracing, *Radio Sci.*, *1*(3), 269–283.
- Lauben, D. S. (1999), Precipitation of radiation belt electrons by obliquely-propagating lightning-generated whistler waves, thesis, Stanford Univ., Palo Alto, Calif.
- Lauben, D. S., U. S. Inan, and T. F. Bell (2001), Precipitation of radiation belt electrons induced by obliquely propagating lightning-generated whistlers, *J. Geophys. Res.*, *106*(A12), 29,745–29,770.
- Leon-Garcia, A. (1994), *Probability and Random Processes for Electrical Engineering*, 2nd ed., Addison-Wesley, Boston, Mass.
- Lundin, B., and C. Krafft (2001), On the similarity features of normalized frequency spectrograms of magnetospherically reflected whistlers, *J. Geophys. Res.*, *106*(A11), 25,643–25,654.
- Mielenz, K. D. (2000), Computation of Fresnel integrals II, *J. Res. Natl. Inst. Stand. Technol.*, *105*(589).
- Neubert, T., T. F. Bell, and L. R. O. Storey (1987), Resonance between coherent whistler mode waves and electrons in the topside ionosphere, *J. Geophys. Res.*, *92*(A1), 255–265.
- Peter, W. B., and U. S. Inan (2004), On the occurrence and spatial extent of electron precipitation induced by oblique nonducted whistler waves, *J. Geophys. Res.*, *109*, A12215, doi:10.1029/2004JA010412.
- Schild, M. A., and L. A. Frank (1970), Electron observations between inner edge of plasma sheet and plasmasphere, *J. Geophys. Res.*, *75*(28), 5401.
- Stix, T. H. (1992), *Waves in Plasmas*, Springer, New York.
- Vette, J. (1991), The AE-8 trapped electron model environment, *Rep. 91-24*, Natl. Space Sci. Data Cent., Greenbelt, Md.
- Walt, M., H. D. Voss, and J. Pickett (2002), Electron precipitation coincident with ELF/VLF wave bursts, *J. Geophys. Res.*, *107*(A8), 1207, doi:10.1029/2001JA009100.
- Wykes, W. J., S. C. Chapman, and G. Rowlands (2001a), Stochastic pitch angle diffusion due to electron-whistler wave-particle interactions, *Phys. Plasmas*, *8*(6).
- Wykes, W. J., S. C. Chapman, and G. Rowlands (2001b), Enhanced phase space diffusion due to chaos in relativistic electron-whistler mode wave particle interactions with applications to Jupiter, *Planet. Space Sci.*, *49*(3–4), 395–404.

T. F. Bell and U. S. Inan, Space, Telecommunications, and Radioscience Laboratory, Department of Electrical Engineering, Stanford University, 350 Serra Mall, Palo Alto, CA 94305, USA.

J. Bortnik, Department of Atmospheric and Oceanic Sciences, University of California, Los Angeles, CA 90095, USA. (jbortnik@gmail.com)